Biomedicine & Pharmacotherapy 198 (2026) 119323

Contents lists available at ScienceDirect

Biomedicine & Pharmacotherapy

journal homepage: www.elsevier.com/locate/biopha

Effective oral countermeasures against ionizing radiation-induced damage without hindering cancer radiotherapy

Rafael López-Blanch [a,1], María Oriol-Caballo [a,b,1], Rosario Salvador-Palmer [b], Paz Moreno-Murciano [a], María Benlloch [c], Juan I. Villaescusa [d], Alegría Montoro [d], Rafel Prohens [e,f], Joan Albertí [f], José M. Estrela [a,b,*], Elena Obrador [a,b,*]

[a] Scientia BioTech, Valencia 46002, Spain
[b] Department of Physiology, Cell Pathophysiology Unit, Faculty of Medicine & Odontology, University of Valencia, Valencia 46010, Spain
[c] Faculty of Medicine & Health Sciences, Catholic University of Valencia San Vicente Martir, Valencia 46001, Spain
[d] IIS and Radioprotection Service, La Fe University and Polytechnic Hospital, Valencia 46026, Spain
[e] Laboratory of Organic Chemistry, Faculty of Pharmacy and Food Sciences, University of Barcelona, Barcelona 08028, Spain
[f] Circe Health Science, Palma 07121, Spain

ARTICLE INFO

Keywords:
Radioprotection
Radiomitigation
Ionizing radiations
Formulated polyphenols
NAD^+ precursors
Captopril

ABSTRACT

High-dose ionizing radiation induces severe multi-organ injury, yet no broadly effective, orally available countermeasure has been validated. Here we describe a fully oral, multi-component formulation comprising bioavailable polyphenol derivatives (pterostilbene cocrystals and silybin-phosphatidylcholine), the NAD^+ precursor nicotinamide riboside, and captopril, an angiotensin-converting enzyme inhibitor with established radiomitigative activity that synergizes with the polyphenols. This combination provides robust systemic radioprotection, enabling long-term survival in 90% of mice exposed to a lethal (LD50/30) dose of X-rays. Mechanistically, the formulation mitigates hematopoietic, intestinal, and neuromotor injury while enhancing DNA repair, suppressing oxidative stress, preserving NAD^+ homeostasis, and activating autophagy. In intestinal epithelial cells, it markedly reduces radiation-induced apoptosis, inflammatory signaling, and mitochondrial dysfunction through coordinated modulation of Nrf2, NF-κB, and sirtuin-regulated stress responses. Critically, normal tissue protection does not compromise tumor control. In triple-negative breast cancer models, irradiation-induced tumor regression is preserved, whereas in glioblastoma (a typically radioresistant malignancy) tumor radiosensitivity is significantly enhanced via sustained oxidative stress, reduced PARP1 expression, and inhibition of HIF-1α and VEGF signaling. Collectively, these findings define an orally deployable, mechanistically integrated strategy that protects normal tissues while preserving or augmenting tumor radiosensitivity, supporting its translational potential as a practical and effective countermeasure against ionizing radiation exposure.

1. Introduction

Exposure to high doses of ionizing radiation, whether accidental, occupational, or therapeutic, can lead to acute radiation syndrome (ARS), a complex and life-threatening condition involving damage across multiple organ systems [1]. In clinical settings, while radiotherapy remains a fundamental modality of cancer treatment, its clinical efficacy is frequently constrained by its adverse effects on healthy tissues [2]. This limitation not only diminishes patient quality of life but also limits the maximum tolerable dose and, consequently, the overall effectiveness of the therapy.

Despite decades of research, no FDA-approved agents currently exist that can be administered preventively to protect against systemic injuries caused by ionizing radiation (IR). In contrast, several radiomitigators, i.e., filgrastim (granulocyte colony stimulating factor, G-CSF), its pegylated form pegfilgrastim, sargramostim (granulocyte-macrophage colony-stimulating factor, GM-CSF), and the thrombopoietin receptor agonist (TPO-Ras) romiplostim have received FDA

* Corresponding authors at: Scientia BioTech, Valencia 46002, Spain.
E-mail addresses: jose.m.estrela@uv.es (J.M. Estrela), elena.obrador@uv.es (E. Obrador).
[1] These authors contributed equally

https://doi.org/10.1016/j.biopha.2026.119323

Available online 6 April 2026

approval for mitigating the hematopoietic form of ARS [3]. These compounds work by counteracting radiation-induced granulocytopenia and thrombocytopenia, thereby reducing the risks of infection and hemorrhage, which are major contributors to ARS-related mortality [4]. However, medical countermeasures capable of preventing or alleviating other manifestations of ARS, including the gastrointestinal and cerebrovascular subtypes as well as the delayed effects of acute radiation exposure (DEARE), remain unavailable, and the protective efficacy of existing agents beyond the acute phase continues to be highly limited. This significant gap underscores the urgent need for effective interventions that can safeguard normal tissues upon exposure to damaging doses of IR.

In a previous work, we demonstrated that I.P. administered natural pterostilbene (PT) and silybin (SIL), in combination with an oral NAD^+ precursor and an I.P administered fibroblast-stimulating lipoprotein 1 (FSL1, a toll-like receptor 2/6 agonist), showed efficacy against harmful doses of γ rays [5]. Nonetheless, the development of an effective, fully oral, radioprotective and radiomitigating formulation has remained a major challenge. Oral compounds offer critical advantages for rapid deployment in emergency situations: they enable self-administration, enhance patient compliance, and minimize the need for specialized medical personnel or equipment. To this aim, we have investigated a strategy that could render systemic protection and be administered orally.

Here, we explore an innovative, fully oral formulation that combines two polyphenol-based compounds -pterostilbene cocrystals (PTCC) and silybin-phosphatidylcholine (SILPC) [6,7], alongside nicotinamide riboside (NR, a vitamin B3 derivative and NAD^+ precursor) [8], and captopril (carboxyphenyl-thiazole, CPT, an angiotensin-converting enzyme inhibitor which has demonstrated radiomitigative effects across multiple tissues, including the hematopoietic system [9], lungs [10], heart [11], and kidneys [12]). Through this work, we aim to advance a practical and scalable approach to radioprotection and radiomitigation, offering critical insights into a formulation with high translational potential for both clinical settings and radiation emergencies.

2. Materials and methods

2.1. Mice and radioprotection/radiomitigation treatment procedures

BALB/c mice (female) were obtained from Charles River Laboratories (Wilmington, MA). Mice were fed a standard laboratory diet (A03 from Panlab, Barcelona, Spain) before irradiation. This diet meets the requirements for adult mice recommended by the American Institute of Nutrition. Mice were fed ad libitum and kept in individual metabolic cages, thus allowing body weight and food ingestion to be monitored daily. The animal room was routinely kept at 22 ºC (12 h light/12 h dark). Care of irradiated mice followed the recommendation of the Robert Wood Johnson Medical School (Piscataway, NJ) for mouse total body irradiation (policy 15), which includes: a) use of antibiotics in the drinking water (134 mg ampicillin/kg/day, 40 mg enrofloxacin/kg/day, and 220/42 mg sulfamethoxazole/trimethoprim/kg/day), b) making drinking water readily available, c) Napa nectar Systems Engineering Lab Group Inc. (Napa, CA) provided on the bottom of the cage during the first 14 days and replaced daily, d) provision of softened food served in a small Petri dish on the cage floor, e) completely sterile environment (cage, food, and water) to avoid potential immunosuppression-associated infections. A freestanding wheel inside the cage was also included to facilitate the physical exercise of the animals.

For irradiations, we used 12-week-old female mice with an approximate weight of 25 g, following the recommendations for harmonized reporting of radiation dosimetry published by Stem, W. et al. [13]. Irradiations were performed at La Fe University and Polytechnic Hospital (Valencia, Spain) using a Varian TrueBeam linear accelerator (Varian Medical Systems, Palo Alto, CA) equipped with an X-ray source operating at 6 MV photon energy in flattened-filtered mode, utilizing a traditional cone-shaped flattening filter to produce a uniform dose distribution. The prescribed dose was 7.2 Gy delivered at a rate of 5 Gy/min, with the absorbed dose to water (Dw) as the reference dose quantity, following the TG-51 calibration protocol of the American Association of Physicists in Medicine. The source-to-surface distance (SSD) was set to 100 cm (the standard source-to-axis distance), and the field size was 40 × 40 cm. Prior to exposure, the linear accelerator was calibrated and verified through a series of procedures ensuring geometric and dosimetric accuracy: IsoCal was used to confirm alignment between the kilovoltage (kV) and megavoltage (MV) imaging systems and the treatment isocenter; MPC (Machine Performance Check) was performed to verify geometric accuracy including source alignment and jaw positions; and TG-51 protocol calibration ensured correct beam output determination in terms of absorbed dose to water. For irradiation, mice were individually restrained in a custom-fabricated Perspex (polymethyl methacrylate) box subdivided into 5 × 5 × 7 cm chambers using 0.5-cm thick Perspex plates, allowing one mouse per compartment to minimize motion and ensure consistent exposure. The chamber array was positioned on the treatment couch with a fixed 100 cm SSD, and irradiation was delivered perpendicularly to the dorsal side of the animals using the 40 × 40 cm field to encompass the entire array. Mice received total body irradiation without shielding or rotation, ensuring consistent geometry and uniform dose distribution across all specimens. X irradiation was performed, as indicated in Fig. 1C, at 10.00 am.

For oral administration, PTCC (Circe Scientific, Mallorca, Spain) and SILPC (indena, Milan, Italy) were solubilized in physiological saline containing 10% 2-hydroxypropyl-β-cyclodextrin, 2% tween 80 and 0.5% carboxymethylcellulose, and the pH of the suspension neutralized before oral administration by gavage (75 mg PT/Kg and 75 mg SIL/Kg). The fine suspension of PTCC and SILPC was maintained by active mixing (vortex) until the moment of its administration. In all cases polyphenols were administered at 9.00 a.m. NR (nicotinamide riboside, 3-aminocarbonyl-1-β-D-ribofuranosyl-pyridinium, Elysium Health, Inc., New York, NY) was dissolved in vaccination-grade water, and the pH of the solution neutralized (pH 7.0) before oral administration (185 mg/Kg x day) [14]. NR was given to the mice using a micropipette tip. CPT (Merck, Darmstadt, Germany) was dissolved in acidified water at 0.55 g/L. NR was administered once per day x 30 days after the irradiation, also including the day of the irradiation. NR was administered at 12.00 am. The dose of CPT administered in the drinking water was calculated to result in an approx. delivery of 110 mg/Kg x day (adjusted daily depending on the variable volume taken by the animals) [9]. CPT was administered x 30 days after the irradiation, also including the day of the irradiation.

All compounds used for *in vivo* treatments were greater than 99% pure by HPLC analysis based on the certificate of analysis provided by the suppliers. PTCC, SILPC and NR were administered once per day (as scheduled in Fig. 1) at 12.00 a.m.

All experiments were conducted using a total of 1264 mice. All animal procedures were performed in strict compliance with the principles of humanity in accordance with the European Community Council Directives (86/609/EEC) and were approved by the Ethics Committee on Animal Use of La Fe University and Polytechnic Hospital, Spain. The appearance of signs of post-irradiation toxicity was monitored daily. Post-irradiation toxicity, which precedes death in fatal cases, can be evidenced by weight loss, cutaneous signs of dehydration, hypothermia, skin inflammation/burns, lethargy, marked pallor (anemia), gastrointestinal bleeding (black stool), and infections. We followed the monitoring protocol proposed by Morton and Griffiths [15]. This monitoring protocol allows the quantification of the suffering caused by a procedure. Five variables are considered (weight loss, appearance, unprovoked behavior, behavior in response to handling, clinical parameters) and each animal is assigned a variable score. Mice were sacrificed at specific times after irradiation (see Results) or as lesions and signs of illness that indicate the animal's discomfort appear. Aside from scheduled sacrifices

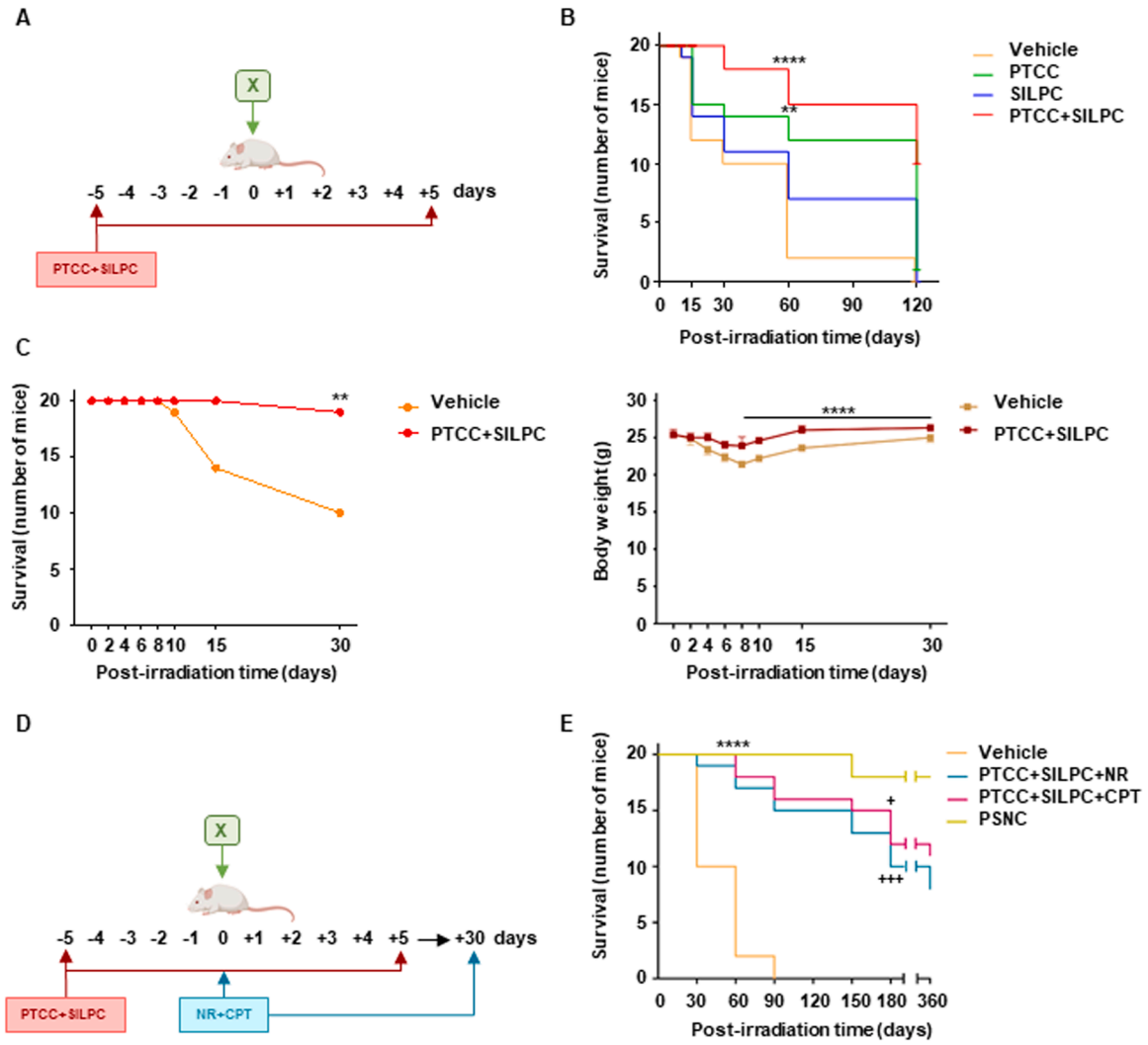

Fig. 1. Effects of PTCC, SILPC, NR, and CPT treatments on the survival of mice subjected to whole-body X irradiation (LD50/30). (**A**) Scheme of the procedure for polyphenol administration. PTCC and/or SILPC (75 mg of each polyphenol/Kg, once per day) as explained under Methods. (**B**) Four-months survival. Mice (n = 20/group) were treated with PTCC and/or SILPC. Data were analyzed with LogRank (Mantel-Cox) test. At day 60, $^{**}P < 0.01$ and $^{****}P < 0.0001$ comparing all experimental groups versus controls (mice treated with vehicle). (C) Effect on body weight versus survival. Kaplan-Meier overall survival curves for irradiated mice treated as in (A) with vehicle or PTCC + SILPC (left); statistical significance between groups (n = 20/group) was determined by the log-rank (Mantel-Cox) test: PTCC + SILPC versus vehicle ($^{**}P < 0.01$). Body-weight changes over time for vehicle- and PTCC + SILPC-treated mice (right) (means ± SD, n = 10–20 per group); statistical significance at each time point was determined by an unpaired, two-tailed Student's t test comparing PTCC + SILPC versus vehicle ($^{****}P < 0.0001$). (D) Scheme of the procedure for drug administration. PTCC and SILPC were administrated as in (A). NR (185 mg/kg x day, one dose per day) was given orally. CPT was given in the drinking water (110 mg CPT/kg/day) (see under Methods). (E) Effect of PTCC, SILPC, NR and CPT on the survival of X-irradiated mice (n = 20/group). PSNC: PTCC + SILPC + NR + CPT. Data were analyzed with LogRank (Mantel-Cox) test: PTCC + SILPC + NR versus vehicle ($^{****}P < 0.0001$), PTCC + SILPC + CPT versus vehicle ($^{****}P < 0.001$), PSNC versus vehicle ($^{****}P < 0.0001$), PSNC versus PTCC + SILPC + NR ($^{+++}P < 0.001$), and PSNC versus PTCC + SILPC + CPT ($^{+}P < 0.05$).

for tissue collection and analysis, mice were not prematurely euthanized unless they met the endpoint criteria indicated above.

2.2. Blood levels of pterostilbene, silibinin and NAD^+

For determination of polyphenols, whole-blood samples (0.5 mL) were collected from the saphenous vein using a 25 G needle, and transferred to sodium citrate tubes at 4 ºC. Then, 0.1 mL were transferred to a cryovial containing 0.9 mL of 0.5 M ice-cold perchloric acid to lyse all cells and, after centrifugation (10,000 g x 10 min at 4 ºC), 0.1 mL of the supernatant was mixed with 400 µL of methyl tert-butyl ether using a vortex. The liquid-liquid extraction was performed using a FM-ARA-B100 automatic liquid extraction rotary agitator (Fison Instruments, Glasgow, UK). Centrifugation (5000*g* x 2 min at 4ºC) was run to separate the organic one. The sample was dried up using a speedvac and resuspended in 100 µL of mobile phase (H_2O and acetonitrile 80:20 v/v, 5 mM ammonium acetate). The mixture was centrifuged x 5 min (5000 g at 4 ºC) to separate the supernatant. An UPLC-MSMS (QqQ) 1290–6460 Agilent (Agilent Technologies, Santa Clara, CA) was used for LC-MS/MS analysis, and 5 µL of sample were injected into an Acquity BEH C18 column (1.7 µm, 2.1 ×100 mm) (Waters, Milford, MA). Eluents were A (H2O + 5 mM ammonium acetate) and B (acetonitrile + 5 mM ammonium acetate). The gradient program was of 80% A/20% B at 0.0–0.5 min, 1% A/99% B at 3.0–4.0 min, and 80% A/20% B at 4.1–5.5 min. The flow rate was 0.3 mL/min and the column temperature was maintained at 40 ºC. The electrospray ionization conditions were: multiple reaction monitoring in negative ion mode, capillary voltage 1 kV. The multiple reaction monitoring mode was employed to monitor both polyphenols with the precursor-to-product ion transition (PT, *m/z* 255.1/240.0; SIL, *m/z* 481.1/300.9). The fragmentary voltage

was 150 V, and the collision energy 20 eV.

To measure NAD^+ levels, whole-blood samples (0.5 mL) were collected in sodium citrate tubes at 4 ºC. Then, 0.1 mL were transferred to a cryovial containing 0.9 mL of 0.5 M ice-cold perchloric acid to lyse all cells and, after centrifugation (10,000 g x 10 min at 4 ºC). NAD^+ was determined by HPLC using a 1290 Infinity III LC System (Agilent Technologies), a Supelco LC-18-T column (15 ×4.6 cm; Merck) and a Hypercarb column (15 ×4.6 cm; ThermoFisher Scientific, Waltham, MA), and following the method of Yoshino and Imai [16].

2.3. Plasma levels of captopril

Whole-blood samples (0.5 mL) were collected (as above) in sodium citrate tubes and centrifuged (1500 g x 10 min at 4 ºC) to collect the uppermost plasma layer. To reduce protein interference, plasma proteins were precipitated by adding 1:1 vol of cold acetonitrile, then the mixture was vortexed for 2 min and centrifuged at 10,000 g x 10 min at 4 ºC. The supernatant was carefully transferred to a clean vial for analysis. The UPLC-MSMS (QqQ) 1290–6460 Agilent was used for LC-MS/MS analysis, and 5 μL of sample were injected into a Cosmosil 5C18-MS-II (5 μm, 2.0 × 50 mm) column. Mobile phase A: H_2O + 0.1% formic acid, mobile phase B: acetonitrile + 0.1% formic acid. The gradient program was of 90% A/10% B at 0.0–2.0 min, 60% A/40% B at 2.0–5.0 min, 20% A/80% B at 5.0–8.0 min, 10% A/90% B at 8.0–10.0 min. The flow rate was 0.2 mL/min and the column temperature was at 40 ºC. The electrospray ionization conditions were: multiple reaction monitoring in positive ion mode, capillary voltage 1 kV. CPT was monitored using the following mass transitions with the electrospray ionization method: CPT - 2, 4′-dibromoacetophenone, *m/z* 416/255. The fragmentary voltage was 150 V, and the collision energy 20 eV.

2.4. 8-hydroxy-2'-deoxiguanosine

Tissue samples were homogenized in 10 mM Tris (pH 7.0) + 1 mM EDTA + 150 mM NaCl, and processed as previously described [17]. Levels of 8OHdG were analyzed by an UPLC-MSMS (QqQ) 1290–6460 Agilent, equipped with a binary solvent manager, an autosampler and a column heater. The column was an ZORBAX Eclipse Plus C18 (1.8 μm, 2.1 mm × 100 mm; Agilent Technologies) and the running temperature at 40 °C. The mobile phase was (A) 0.1% acetic acid, and (B) methanol. An isocratic mode was used to achieve the desired sample separation using 92.5% A and 7.5% B with a flow rate of 0.3 mL/min. The injection volume was of 5 μL. The flow from the column was directed to the mass spectrometer.

2.5. Isoprostanes

Tissue samples were homogenized in 0.1 M phosphate buffer (pH 7.4) + 1 mM EDTA + 0.005% butylated hydroxytoluene. Isoprostanes were measured using the 8-isoprostane EIA kit (Cayman Chemical Co.) and following the manufacturer's protocol.

2.6. Protein carbonyls

Carbonylation of proteins was measured using the Protein Carbonyl Fluorometric Assay Kit (Cayman Chemical Co.) and based on the manufacturer's protocol.

2.7. Chromosomal aberrations, double-strand DNA breaks and micronuclei

We followed the technique described by M'kacher et al. [18]. Blood (1.0 mL) was collected (as above) 12 h after irradiation, thus allowing time for DNA repair and the occurrence of chromosomal aberrations. Blood mononuclear cells were obtained from heparinized blood by ACCUSPIN™ System-Histopaque®-1077 (Merck) gradient centrifugation. Positive selection of lymphocyte subsets by Dynabeads® Pan Mouse IgG magnetic bead separation technology (Thermo Fisher Scientific) was performed at 4 ºC following manufacturer's instructions. Isolated lymphocytes were incubated (10^6 cells/flask) at 37 ºC in Krebs-Ringer medium with 5% fat-free bovine serum albumin and in the presence of glucose (5 mM) and glutamine (2 mM). Cytogenetic damage was quantified by a premature chromosome condensation (PCC)-based assay, using CHO cells (ATCC) [19]. The condensed chromosomes were differentiated from the CHO chromosomes according to their morphology [18]. Telomeres and centromeres of PCC fusions were stained using the Q-FISH technique [18]. For PCC, lymphocytes were processed using a PCC fusion protocol and stained with telomere and centromere peptide nucleic acid probes to facilitate detection of dicentrics, centric rings, and acentric fragments. For each mouse, 50 PCC spreads were scored, and results are reported as dicentrics per cell, with group means calculated from per-animal means. Dicentrics were defined as chromosomes containing two centromeres with accompanying telomeric signal patterns consistent with fusion, centric rings as ring structures containing a centromere, and acentric fragments as fragments lacking centromeric signals, following standardized scoring criteria. Slides were coded and scored by blinded analysts. Telomere and centromere-stained fusions were automatically recorded using the Autocapt software from Metasystems (Altlussheim, Germany) and a high-resolution CCD camera (C91002–23B, Hamamatsu Photonics, Herrsching, Germany).

In the same slide two different manual procedures were performed based on M'kacher et al. [18]. Briefly, using first the reverse 4',6-diamidino-2-phenylindole, and scoring rings and excess acentric chromosomes. Second, using the telomeres and centromeres staining to score dicentrics, centric rings, and acentric chromosomes. Resulting DSBs were calculated [18].

For micronuclei detection, the femoral bone marrow was collected, and smear was fixed utilizing methanol. After drying, a double staining with May Grunwald and Giemsa stains was prepared [20]. According to this method, PCE stained reddish-blue and NCE stained orange, while nuclear materials were dark purple.

The MnPCE and MnNCE cells were counted out of 2000 cells under oil immersion.

2.8. Isolation and incubation of hepatocytes, intestinal epithelial cells, and brain neurons

Isolation and incubation of hepatocytes followed previously reported methodology [21].

Primary IEC were isolated using colon tissue and the methodology of Graves et al. [22]. The isolated intestinal crypts were suspended in the complete growth media (DMEM, 8.5 g/l sodium pyruvate, 2% v/v FBS, 0.25 U/mL insulin, 100 U penicillin, 100 lg/mL streptomycin, 25 μg/mL gentamycin, 5 μg/mL transferrin, and 10 ng/mL EGF containing 2% w/v D-sorbitol), plated at a density of approx. 2000 crypts/mL/well in type I collagen-coated culture dishes (Thermo Fisher Scientific), and incubated at 37 ºC.

To isolate adult brain neurons, we followed the methodology described by Brewer and Torricelli [23]. Briefly, we started with cortex dissection and digestion with papain at 30 ºC. Then, purification of neurons on density gradient (OptiPrep™ Density Gradient Medium, Merck) and resuspension in Neurobasal/B27 medium (25 mL NeurobasalA, 0.5 mL B27, 0.5 mM L-Gln, 10 μg/mL gentamycin) (Invitrogen, Waltham, MA) supplemented with 5 ng/mL mouse FGF2 plus 5 ng/mL mouse PDGFbb. Isolated neurons were plated on a poly-Lys-coated Corning® VISTA™ Petri Dish (Merck).

2.9. Comet assay

The percentage of fragmented DNA that has migrated away from the nucleus (% DNA in tail) was determined by confocal microscopy (LEICA

TCS-SP8, Wetzlar, Germany) and using the assay kit from Abcam (ab238544) (Cambridge, UK) according to the manufacturer's instructions. Briefly, cells were resuspended in ice-cold PBS (without Ca^{2+}/Mg^{2+}) at ~1 × 10^5 cells/mL and mixed with molten comet agarose (37 ºC) at a 1:10 ratio (v/v). A total of 75 μL of the mixture was pipetted onto comet slide wells containing a base agarose layer and allowed to solidify for 15 min at 4 ºC in the dark. Slides were incubated in pre-chilled lysis buffer for 30–60 min at 4 °C and then transferred to alkaline unwinding solution (300 mM NaOH, 1 mM EDTA; pH > 13) for 30 min at 4 ºC. Electrophoresis was performed in alkaline buffer (300 mM NaOH, 1 mM EDTA) at ~1 V/cm for 15–30 min with a current of ~300 mA. Following electrophoresis, slides were washed three times with cold distilled water (2 min each), incubated in 70% ethanol for 5 min, and air-dried at 37 ºC for 30 min. DNA was stained with fluorescent dye (100 μL/well, 15 min, room temperature, dark) and visualized by epifluorescence microscopy using a FITC filter. For each mouse, 100 nucleoids were scored across 2 gels per slide, and % DNA in tail was computed using Comet Assay IV software. Apoptotic "hedgehog" comets were excluded from quantitative analysis and recorded separately.

2.10. Pathology: bone marrow, intestine

Bone marrow cells were flushed from isolated femurs using 26-gauge needle with pre-chilled PBS. The number of viable bone marrow nucleated cells was assessed using a TC20 Automated Cell Counter (Bio-Rad, Hercules, CA).

Femurs and jejunums were isolated and fixed in 4% paraformaldehyde for 48 h and then embedded in paraffin. Sections were cut in 4 μm of thickness and used for hematoxylin and eosin staining. These sections were visualized using a Leica DMD108 microscope (Leica Microsystems, Wetzlar, Germany).

2.11. Colony forming cells in the bone marrow

Bone marrow cells were flushed from the isolated femurs with PBS (4 ºC) containing 5% fetal bovine serum. Single-cell suspension was passed through 100 μm nylon mesh strainer to remove debris and clumps. Cells were washed twice with PBS (4 ºC) and counted in the TC20 Automated Cell Counter. Cells were plated at a concentration of 5 × 10^4 cells per 35 mm cell culture dish in Methocult GF M3434 (Stemcell Technologies, Vancouver, Canada) growth medium and incubated for 14 days at 37 ºC. Colonies were visualized on day 14 of culture using light microscopy (Leica DFC7000T) under a polarized light and scanned in a 60 mm gridded scoring Petri dish (Stemcell Technologies). Hematopoietic colony forming CFU-GM and CFU-GEMM cells were quantified.

2.12. Evaluation of in vivo toxicity

Blood hematology and chemistry measurements followed standard clinical methodology [24,25].

2.13. Automatic evaluation of neuromotor activity

Changes over time in spontaneous activity (locomotion) were measured by means of an Infrared Motion Sensor Activity Monitor (IR Actimeter, Harvard Apparatus, Hill Road Holliston, MA). The IR Actimeter is composed by a two-dimensional (X and Y axes) square frame, a frame support, and a control unit. Each frame is composed of 16 × 16 infrared beams for optimal subject detection. It works by using IR sensors that track the movement of the animal within the monitored area. Activity was expressed as the time (in seconds) moving slow (time during which the subject speed is between the resting and the fast thresholds, 2–5 cm/s) or moving fast (time during which the speed of the subject is above the fast threshold, >5 cm/s). Resting period was considered the time period during which the speed of the subject is below the resting threshold (<2 cm/s). The register was performed in blocks of 2-min during the observation time period (30 min). Changes over time in the different groups were monitored weekly.

2.14. Immortalized intestinal epithelial cells and in vitro X irradiation

Immortalized CI-muADINTESTI murine adult IEC were from InSCREENeX GmbH (Brunswick, Germany). For *in vitro* irradiation we used a Cellrad - Benchtop X-Ray Irradiator (PRECISION X-RAY IRRADIAION, Madison, CT).

2.15. Cell death analysis in vitro

Apoptotic and necrotic cell death were distinguished by using fluorescence microscopy. For this purpose, isolated cells were incubated with Hoescht 33342 (10 mM; which stains all nuclei) and propidium iodide (10 mM; which stains nuclei of cells with a disrupted plasma membrane), for 3 min, and analyzed using a Diaphot 300 fluorescence microscope (Nikon, Tokyo, Japan) with excitation at 360/537 nm, respectively. Nuclei of viable, necrotic, and apoptotic cells were observed as blue round nuclei, pink round nuclei, and fragmented blue or pink nuclei, respectively.

2.16. RT-PCR analysis

For this procedure, 10^5 cells were mixed with lysis solution (Thermo Fisher Scientific) and incubated x 5 min at room temperature to lyse the cells and remove gDNA. Then, the stop solution (Thermo Fisher Scientific) was added and incubated x 2 min. Samples were stored at −80ºC. Real time quantitation of each mRNA relative to glyceraldehyde-3-phosphate dehydrogenase (gapdh) mRNA was performed with a SYBR Green I assay and an iCycler detection system (Bio-Rad). Target cDNAs were amplified in separate tubes as follows: 10 min at 95 °C and then 40 cycles of amplification (denaturation at 95 °C x 30 s, and annealing and extension at 60 °C x 1 min per cycle). PCR master mix and AmpliTaq Gold DNA polymerase (Applied Biosystems, Waltham, MA) were added to the specific primers (Agilent Tecnologies), which were those previously reported for sod2, cat, gpx2, gr, txnrd1, hmox2, sirt1 and sirt3, and gapdh [14]. Other primers used are displayed in Table S2. The increase in fluorescence was measured in real time during the extension step. The threshold cycle (C_T) was determined, and then the relative gene expression was expressed as follows: fold change = $2^{-\Delta\,(\Delta CT)}$, where ΔC_T = C_T target - C_T glyceraldehyde-3-phosphate dehydrogenase, and Δ (ΔC_T) = ΔC_T treated - ΔC_T control.

2.17. Cytokines

The simultaneous quantification of cytokines in plasma was performed using xMAP technology and a MAGPIX Luminex 200 platform (Thermo Fisher Scientific). Briefly, after the incubation of a specific monoclonal antibody conjugated bead population with 50 μL of plasma samples for 1 h (room temperature), washed beads (color-coded beads of specific monoclonal antibodies) were incubated with detection antibody solution for 30 min, then with the streptavidin–phycoerythrin-conjugated solution (10 min). After washing, the beads were resuspended in the assay buffer, shaken for 1 min, and then read on the MAGPIX instrument. The results were analyzed with xPONENT 4.2® software and expressed as picograms per mL.

2.18. Western blots

Cells were washed twice with PBS, and the pellet was suspended in ice-cold homogenization buffer (2 ×106 cells per mL of buffer: 20 mM HEPES pH 7.5, 250 mM sucrose, 1 mM $MgCl_2$, 10 mM KCl, 1 mM EDTA, 1 mM EGTA, 1 mM dithiothreitol, 0.1 mM phenylmethylsulfonyl fluoride, and 10 mg leupeptin, aprotinin, and pepstatin A/mL). Proteins were quantified [26], separated by SDS-PAGE, transferred to PVDF

membranes, and subjected to western blotting. The following monoclonal antibodies were used: Anti-SOD1 (ab51254, abcam), anti-SOD2 (ab68155, abcam), anti-CAT (ab209211, abcam), anti-GPX1 (ab22604, abcam), anti-TXNRD1 (67728–1-Ig, Prointech, Gentofte, Denmark), anti-BCL2 (sc-7382, Santa Cruz), anti-BCLXL (ab32370, abcam), anti-BAX (ab32503, abcam), anti-CytC (ab133504, abcam), anti-AIF (ab32516, abcam), anti-PUMA (MA4800, Apexbio, Houston, TX), anti-P-NRF2 (PA5–27882, Invitrogen), anti- NF-kBp65 (D14E12, Cell Signaling Technology, Danvers, MA), anti-cMYC (sc-40, Santa Cruz Biotechnology), anti-PARP1 (MA5–15031, Invitrogen), anti-LC3-II (81004–1-PR, Prointech), anti-P62/SQSTM1 (M00300, Boster Bio, Pleasanton, CA), anti-SIRT1 (MA5–27217, Invitrogen), and anti-SIRT3 (PA5–86035, Invitrogen). The internal standard (5 μM/well) was from Thermo Scientific (ref. 26623). As a loading control, we used tubulin (ab7291, abcam) or lamin B1 (ab229025, abcam). Blots were developed using an anti-rabbit or anti-mouse horseradish peroxidase-conjugated secondary antibody and enhanced chemiluminescence (ECL system; GE HealthCare Life Sciences, Uppsala, Sweden). Protein bands were quantified using laser densitometry. To make the pooling of data from different immunoblots possible, the relative density of each band was normalized against the internal standard analyzed on each blot.

2.19. Gene silencing and autophagy test

The PSilencer 3.1-H1 linear vector from Ambion Inc. (Austin, TX) was used to obtain long term gene silencing. To target mouse Nfkbie, a murine shRNA (Cat. No: shAAV-265728) from vector biolabs (Malvern, PA) was used. The shRNA to target mouse Nfe2l2 (Locus ID 18024) was from Origen (Rockville, MD). In all cases silencing procedures followed the technical recommendations of the manufacturers. In the control experiments we used equivalent amounts of the corresponding sense oligonucleotides and scrambled oligonucleotides with the same base composition and a randomized sequence. Silencing was confirmed by immunoblotting. TransFectin™ Lipid Reagent (Bio-Rad) and manufacturer's protocol was used for delivery of shRNA.

The autophagy assay kit ab139484 from abcam was used, following manufacturer's instructions, for the fluorescence detection of autophagic vacuoles.

2.20. Cancer cell culture and orthotopic inoculation

Human MDA-MB-436 carcinoma and U-87 GB cells, as well as their normal counterparts (MCF-10A and SVG p12 cells) were from the ATCC. Cells were grown in DMEM (Invitrogen), pH 7.4, supplemented with 10% heat-inactivated FBS (Biochrom KG), 100 units/mL penicillin and 100 μg/mL streptomycin. Cells were plated (20,000 cells/cm^2) and cultured at 37 °C in a humidified atmosphere with 5% CO_2. Cells were harvested by incubation for 5 min with 0.05% (w/v) trypsin (Merck) in PBS, pH 7.4, containing 0.3 mM EDTA, followed by the addition of 10% FBS to inactivate the trypsin. Cells were allowed to attach for 12 h before any treatment addition. Cell number and trypan blue exclusion-based viability were determined using the Bio-Rad TC20 Automated Cell Counter. Cell integrity was also confirmed by measuring leakage of lactate dehydrogenase activity.

Nude (nu/nu) mice (male, 9–10 weeks old, approximate weight of 25 g) (Charles River Laboratories), were fed *ad libitum* on a standard diet (Letica), and kept on a 12-h-light/12-h-dark cycle with the room temperature at 22 °C.

To generate orthotopic MDA-MB-436 carcinomas, mice were implanted with 2×10^6 cells into the mammary fat pad of an animal. Tumor volume was measured using calipers and expressed in mm^3 according to $V = 0.5a \times b^2$ (where a and b are the long and short diameters, respectively).

For grafting of U87 cells, five μL of cell suspension (approx. 3×10^5 cells) were intracerebrally injected into the left hemisphere of experimental animals. The dynamics of the tumor growth were studied by means of magnetic resonance imaging on a high field BioSpec 94/20 USR tomograph (Bruker, Germany), and based on previously described methodology [27]. Studies were conducted on the animals narcotized by isoflurane (1.5% isoflurane in the oxygen mixture at a flow rate 250 mL/min). Post-mortem histological examination was used to evaluate the final tumor size.

Xenografted tumors were allowed to grow for 4 (U87)-6 (MDA-MB-436) weeks and then were surgically removed. The sacrifice was performed by cervical dislocation. For histological analysis, tumors were fixed in 4% formaldehyde in PBS (pH, 7.4) for 24 h at 4 °C, paraffin embedded, and stained with hematoxilin-eosin and safran. Cell proliferation was detected using anti-Ki67 monoclonal antibodies (ab92742, abcam).

2.21. Isolation of cancer cells from in vivo growing tumors

Cell dispersion was carried out in minced tissues by the following a sequential procedure: 1) trypsinization (approx. 25 mg of fresh tissue per mL in Mg^{2+} and Ca^{2+} free PBS supplemented with 0.2% trypsin plus 0.5 mM EDTA plus 5 mM glucose, 3 min at 37 °C); 2) three washes in PBS; 3) collagenase digestion (in PBS supplemented with 0.5 mg of collagenase/mL plus 5 mM glucose, 5 min at 37 °C) (steps 1 and 3 were performed in Erlenmeyer flasks where the gas atmosphere was O_2/CO_2, 19:1). Then, cells were washed three times in PBS, passed through a 30 μm nylon mesh to remove clumps, and resuspended in 80 μL DMEM (approx. 10^7 total cells) plus 20 μL of non-tumor cell depletion cocktail (which contains a cocktail of monoclonal antibodies conjugated with MACS® MicroBeads to allow removal of all non-tumor cells i.e., lymphocyte subpopulations, fibroblasts, and endothelial cells; Miltenyi Biotec, Auburn, CA). Cell suspension was incubated x 15 min at 4°C. Cell suspension volume was adjusted to 500 μL with DMEM and used for magnetic separation using a Multi-24 column and a MultiMACS Cell24 separator. We followed the protocol and recommendations of the manufacturer (Miltenyi Biotec). The flow-through containing unlabeled cells, corresponding to the enriched tumor cell pool (>95%), was collected. To isolate pure cancer cell fractions (thus eliminating parenchyma cell contamination), cancer cells were labeled with anti-TNBC antibody [Mesothelin Monoclonal Antibody (clone 5B2), abcam, EPR19025–42] or anti-U87 antibody (Tenascin 81C6 Monoclonal Antibody, abcam, EPR4219), separated by flow cytometry cell sorting (BD FACSAria™ Fusion Flow Cytometer, BD Biosciences), and plated in 25-cm^2 polystyrene flasks (Falcon Labware) as above.

2.22. Hydrogen peroxide and superoxide

The assay of H_2O_2 production was based on the H_2O_2-dependent oxidation of homovanillic acid (4-hydroxy-3-methoxyphenylacetic acid) to a highly fluorescent dimer (2,2'-dihydroxydiphenyl-5,5'-diacetic acid), which is mediated by horseradish peroxidase [28]. For this purpose, cells were cultured in the presence of 100 μM homovanillic acid and 1 unit/mL horseradish peroxidase. A linear relationship between fluorescence (λex= 312 nm and λem= 420 nm) and amount of H_2O_2 was found in the range of 0.1–12 nmol/2-mL assay

Generation of O_2^- was quantitated using an electrochemical biosensor as previously described [29]. Briefly, A $Co_3(PO_4)_2$ nanorod/glassy carbon electrode was applied to in situ electrochemically detect O_2^- released from isolated IEC (5×10^5 cells/mL) in real time. In order to ensure accuracy of measured O_2^- concentrations, cell culture medium inside the device was mildly stirred during cell released O_2^- measurement. The electrochemical measurements were carried out on a CHI760 electrochemical workstation (CH Instruments Inc., Austin, TX).

2.23. Mitochondrial membrane potential

Quantitative determination of the MMP was performed by the uptake of the radiolabeled lipophilic cation methyl triphenylphosphonium

(TPMP), which enables small changes in potential to be determined [30]. Briefly, cells (2×10^6) were incubated at 37 ºC for 60 min in 1 mL DMEM, supplemented as mentioned above but including 1 μM TPMP, 250 nCi ^{3}H-TPMP (Amersham, Bucks, UK), and 1 μM sodium tetraphenylboron. After incubation, the cells were pelleted by centrifugation (1000 x g for 5 min), 100 μL of the supernatant were removed, the pellet resuspended in 100 μL 10% Triton X-100, and the radioactivity (disintegrations/min) was measured using a Tri-Carb Liquid Scintillation Counter from Perkin-Elmer. Non-specific TPMP binding was corrected as previously described [30]. Energization-dependent TPMP uptake was expressed as an accumulation ratio in units of [(TPMP/mg protein)/(TPMP/μl supernatant)] [31].

2.24. Ki67, VEGF, and HIF-1α

Quantitative determination of Ki67, as a cellular marker for proliferation, was carried out by immunohistochemistry and positive cell counting (anti-Ki67 polyclonal antibody was from abcam, ab15580); whereas for quantitative determination of VEGF and HIF-1α we used specific human ELISA kits from abcam (VEGF, ab100662; HIF-1α, ab171577).

2.25. Statistical analysis

Statistical analyses were performed using Prism 10.0 software (GraphPad Prism). Data are presented as means ± SD. For survival analysis, 15 and 30-day survival proportions were compared using two-tailed Fisher's exact test, while Kaplan–Meier curves were analyzed by the log-rank (Mantel–Cox) test. Longitudinal changes in body weight and tumor growth were analyzed by two-way repeated-measures ANOVA (treatment × time), followed by Bonferroni's multiple comparisons at individual time points. One-way ANOVA with Bonferroni's post hoc test was used for multi-group comparisons (e.g., molecular markers, cytogenetic abnormalities, hematopoietic colonies, cytokine levels, and crypt measurements); Dunnett's T_3 test was applied when variances were unequal. Unpaired two-tailed Student's t tests were used for comparisons between two groups when appropriate. Statistical significance is indicated as $P < 0.05$, $P < 0.01$, $P < 0.001$, and $P < 0.0001$, as detailed in figure legends.

3. Results

3.1. Combination of radioprotectors and radiomitigators promotes long-term survival of whole-body irradiated mice

We first investigated the effects of orally administered radioprotectors (PTCC and SILPC) on the survival of mice exposed to an LD50/30 dose of X rays. To determine optimal dosing, we tested a range from 0 to 150 mg/kg for each polyphenol. In control mice, mortality reached 50% by day 30 post-irradiation (Fig. S1). Treatment with 75 mg/kg of PTCC reduced mortality by four animals, while the same dose of SILPC reduced it by only one (n = 20 mice; Fig. S1). Increasing the dose to 100 mg/kg did not yield further improvement (Fig. S1), indicating that 75 mg/kg appeared as the most effective and, thus, was selected for subsequent experiments.

The combination of PTCC and SILPC (given for five days before and five days after X irradiation, Fig. 1A) significantly enhanced survival: while only 50% of control mice survived to day 30, survival increased to 90% in the treated group (Fig. 1B). Notably, no control mice survived beyond 120 days, whereas 50% of the polyphenol-treated mice did (Fig. 1B). This variability (50% vs. 90%, Fig. S1 and Fig. 1B) makes it possible to detect partial protection by the formulation. In contrast, a higher radiation dose raises mortality among controls, resulting in too few survivors to allow a valid comparison. (Fig. S2).

In terms of body weight, control mice lost approximately 16% within 8 days of irradiation, although surviving animals recovered by day 30 (Fig. 1C). In contrast, polyphenol-treated mice showed only a 6% weight loss (Fig. 1C), suggesting a protective effect on overall health and recovery.

Next, we examined whether adding two potential radiomitigators, NR and CPT, also administered orally, could enhance the protective effects of the PTCC and SILPC combination. As illustrated in Fig. 1D, polyphenols were given for five days before and five days after X irradiation, while NR and CPT were administered daily for 30 days, beginning two hours post-irradiation. This fully oral treatment regimen markedly improved survival: 90% of irradiated mice survived for up to one year, compared to 0% survival beyond 90 days in the vehicle-treated controls (Fig. 1E). In contrast, treatment with NR and/or CPT alone only modestly increased survival in mice exposed to the LD50/30 radiation dose (Fig. S3).

Fig. S4 shows the blood levels of PT, SIL, and NAD^+, as well as the plasma levels of CPT, in treated mice. Notably, administration of the formulated compounds PTCC and SILPC resulted in significantly higher blood levels of PT and SIL compared to their natural forms, demonstrating improved bioavailability.

3.2. Formulated polyphenols reduce molecular and cytogenetic damage caused by radiation induced-oxidative stress

To assess the radioprotective effects of the formulated polyphenols, we examined first their ability to reduce radiation-induced cellular damage. As shown in Fig. 2, we measured 8-hydroxy-2'-deoxyguanosine (8-OHdG) (Fig. 2A), 8-isoprostane (Fig. 2B), and protein carbonyls (Fig. 2C) as biomarkers of DNA, protein, and lipid oxidation, respectively. These measurements were conducted in different cell types isolated from control mice, X-irradiated mice, and X-irradiated mice pretreated with polyphenols. Across all studied cell types -including circulating $CD2^+$ lymphocytes ($CD2^+L$), hepatocytes (HEP), intestinal epithelial cells (IEC), and cortical neurons (CN)- the formulated polyphenols significantly reduced radiation-induced molecular damage.

In parallel, we measured various cytogenetic parameters in circulating $CD2^+L$ to assess radiation-induced chromosomal alterations, which are widely used for monitoring exposure to IR. These include the number of dicentrics (abnormal chromosomes with two centromeres instead of one) (Fig. 2D), ring chromosomes (which form when both ends of a single chromosome break and then rejoin in a circular shape) (Fig. 2E), and acentric fragments (chromosome pieces that lack a centromere) (Fig. 2F). Additionally, we evaluated DNA strand breaks (Fig. 2G) and the formation of micronuclei (extranuclear bodies arising from acentric fragments or whole chromosomes that fail to integrate into the main nucleus during cell division) (Fig. 2H). $CD2^+$ cells represent a well-established population enriched in T and NK lymphocytes, which are the standard cell type for measuring radiation-induced chromosomal aberrations and double-strand breaks (DSBs). Their radiosensitivity and stable accessibility in peripheral blood make them the most commonly used cell population for cytogenetic biodosimetry. As shown in Fig. 2, all these radiation-induced alterations were significantly reduced in irradiated mice pretreated with PTCC and SILPC. The observed dicentric yields reflect acute high-dose-rate irradiation and PCC-enabled detection of unstable aberrations at high doses, which can yield higher apparent frequencies than conventional metaphase scoring in stimulated lymphocytes due to differences in cell-cycle dependence and aberration detectability. The concomitant administration of PTCC + SILPC + NR + CPT (shorten as PSNC) did not significantly change any of the results shown in Fig. 2 (not shown).

3.3. Addition of radiomitigators enhance DNA repair and promote hematopoietic, intestinal and neuromotor recovery

As shown in Fig. 3A, NR treatment increases NAD^+ content across different cell types and prevents the NAD^+ depletion induced by X-ray radiation. PTCC + SILPC or CPT, when administered alone, did not alter

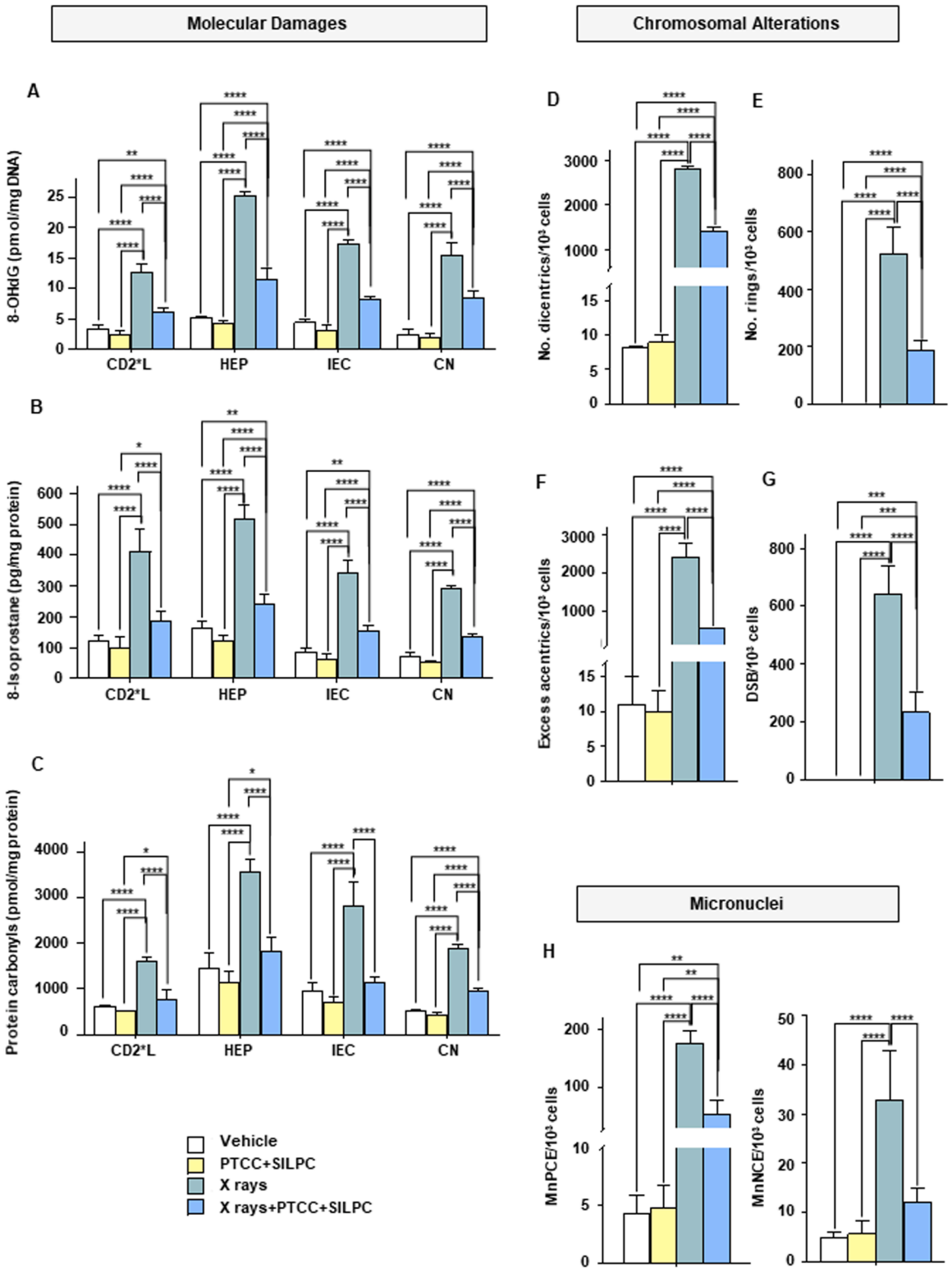

Fig. 2. Protective effect of PTCC and SILPC on the X radiation-induced oxidative and cytogenetic damage. Effect of PTCC + SILPC on the levels of different oxidative damage-related molecular markers (**A, B, C**) in cells ($CD2^+L$, HEP, IEC and CN) isolated from control and X-irradiated mice. Formulated polyphenols (administered five days previously to irradiation and five days after irradiation) and X rays (LD50/30) were administered as indicated under Methods (n = 5 per group, cell type, and treatment). Data are means ± SD. Statistical analysis for each cell type was performed using one-way ANOVA followed by Bonferroni's multiple-comparisons test (*$P < 0.05$; **$P < 0.01$; ****$P < 0.0001$). Effect of *P*TCC + SILPC on the X radiation-induced chromosomal aberrations (**D, E, F, G**) and micronuclei formation (**H**) in circulating $CD2^+L$. Lymphocytes were isolated from mice (n = 5 per experimental group) and procedures were as described under Methods. DSBs, double-strand DNA breaks; MnPCE, micronucleated polychromatic erythrocytes; MnNCE, micronucleated normochromatic erythrocytes. All measurements were performed 48 h after irradiation. Data are means ± SD. Under each type of chromosomal alteration, groups were compared by one-way ANOVA followed by Bonferroni's multiple-comparisons test (**$P < 0.01$; ***$P < 0.001$; ****$P < 0.0001$).

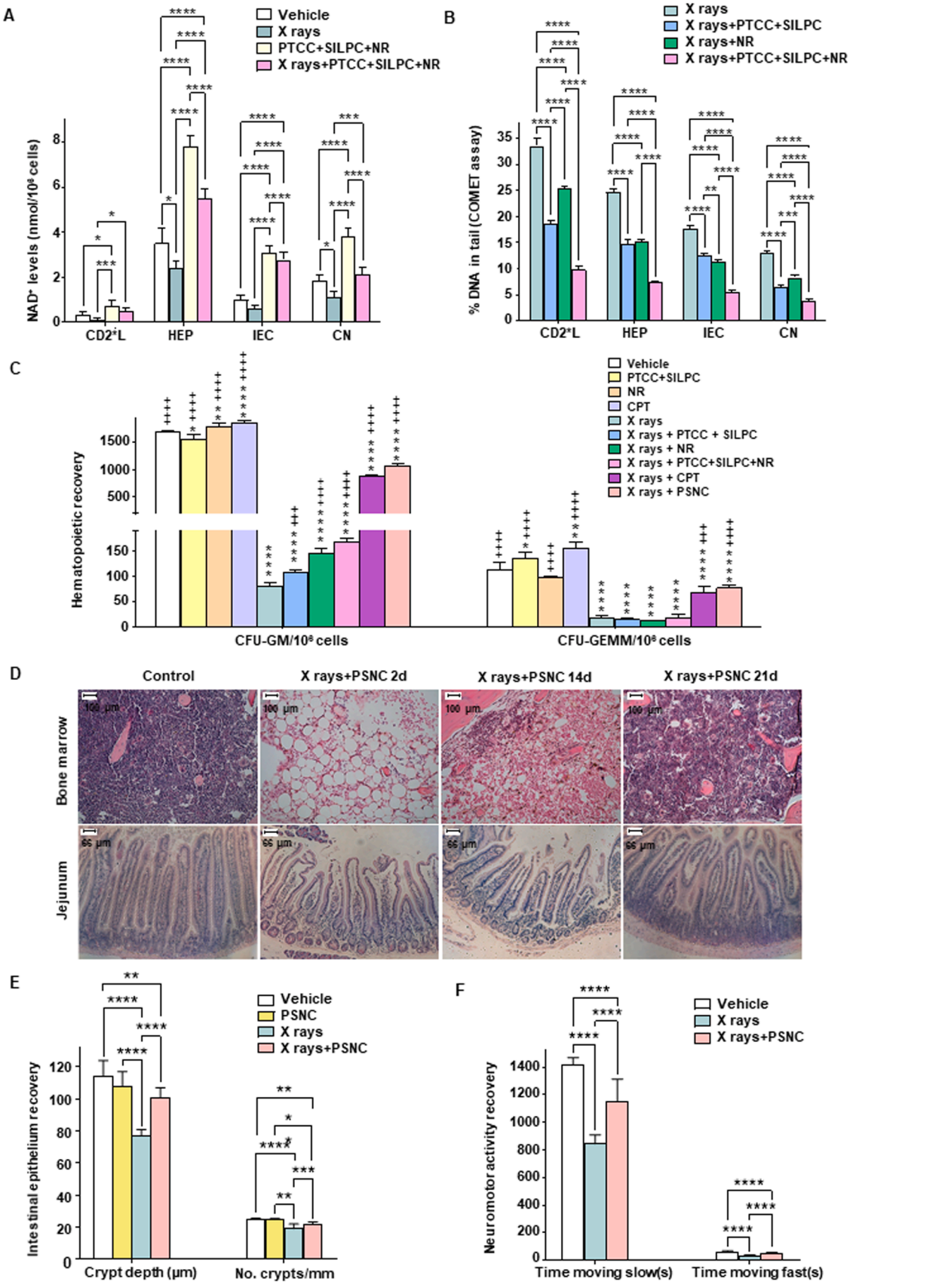

(caption on next page)

Fig. 3. Effects of the oral radioprotective and radiomitigating formulation on DNA damage, and hematopoietic, intestinal and neuromotor recovery in mice exposed to whole-body X-irradiation (LD50/30). (**A**) Effect of PTCC, SILPC and NR on the NAD^+ content of cells isolated from X-irradiated mice (n = 5 per group, cell type, and treatment). Cells were isolated 5 days after irradiation (see the treatment protocol in Fig. 1C). Data are shown as means ± SD. Statistical analyses were performed using one-way ANOVA followed by Bonferroni's post hoc test. $^*P < 0.05$, $^{***}P < 0.001$, $^{****}P < 0.0001$. (B) Effect of PTCC, SILPC, and NR (administered as in Fig. 1C) on DNA damage in cells isolated from X-irradiated mice (n = 5 per group, cell type, and treatment). Cells were isolated from treated mice 5 days after irradiation. Baseline DNA damage corresponds to the irradiated control group (X rays). Data are shown as means ± SD. Statistical analyses were performed using one-way ANOVA followed by Bonferroni's post hoc test ($^{**}P < 0.01$, $^{***}P < 0.001$, $^{****}P < 0.0001$). (C) Effect of PTCC, SILPC, NR and CPT on the hematopoietic recovery of X-irradiated mice. CFU-GM and CFU-GEMM hematopoietic colony forming cells were quantified in femurs isolated from control and treated mice (n = 5 per group and treatment). Mice were treated as in Fig. 1 and bone marrow cells isolated 14 days after irradiation. Data are presented as means ± SD. Statistical analyses were performed using an unpaired two-tailed t test comparing each group versus controls (vehicle) ($^*P < 0.05$, $^{**}P < 0.01$, $^{***}P < 0.001$, $^{****}P < 0.0001$) and to the X-ray group ($^{+++}P < 0.001$, $^{++++}P < 0.0001$). (D) Bone (femurs) and intestinal (jejunum) histopathology was performed on days 2, 14 and 21 after irradiation (representative images shown). (E) Depth and number of intestinal crypts (jejunum). Mice were sacrificed by cervical dislocation on the day 21 post-irradiation. Tissues were processed and analyzed as described under Methods. Data represent means ± SD for 10 different animals per experimental group. Statistical analyses were performed using one-way ANOVA followed by Bonferroni's post hoc test ($^{**}P < 0.01$, $^{***}P < 0.001$, $^{****}P < 0.0001$). (F) Neuromotor activity was evaluated 21 days post-irradiation as indicated under Methods. Data represent means ± SD for 10 different mice per group. Statistical analyses were performed using one-way ANOVA followed by Bonferroni's post hoc test ($^{****}P < 0.0001$).

NAD^+ levels in any of the studied cells and had no significant impact on the NR-induced increase (not shown). Based on the DNA damage COMET assay, both PTCC + SILPC and NR contributed to DNA repair, with their combination being the most effective (Fig. 3B). The data in Fig. 2A-C suggest that polyphenols may exert their effects through antioxidant mechanisms, while the NR-mediated increase in NAD^+ levels (Fig. 3A) may directly promote DNA repair activity (Fig. 3B). In this, it is important to remark that NR enhances post-acute irradiation DNA repair capacity but does not alter the irreversible chromosomal aberrations formed during the first cell cycles after irradiation. This explains why NR-mediated improvements observed in Fig. 3 do not modify the chromosomal instability markers measured at 48 h in Fig. 2. Moreover, while data are consistent with improved DNA repair, they could also reflect lower initial DNA damage in the NR group.

As illustrated in Fig. 3C, CPT selectively promotes the formation of hematopoietic colony-forming units, including CFU-GM (granulocyte-macrophage) and CFU-GEMM (granulocyte-erythroid-macrophage-megakaryocyte), aligning with post-irradiation hematopoietic recovery, as indicated by the hematology data reported in Table S1. Bone marrow recovery elicited by the radioprotecting/radiomitigating formula (PSNC) is illustrated in Fig. 3D. Administration of the PSNC formula also enhanced jejunal crypt depth and number (Fig. 3E; see also the histopathological images in Fig. 3D) and improved neuromotor activity recovery in X-irradiated mice (Fig. 3F).

These findings indicate that the combination of proposed radioprotectors and radiomitigators represents a promising strategy to counter radiation-induced damage. By preserving NAD^+ levels, promoting DNA repair, supporting hematopoiesis, and enhancing tissue and neuromotor recovery, this approach may improve outcomes in individuals exposed to radiation.

3.4. *Molecular interactions underlying the effect of the radioprotective/radiomitigating formula*

Our findings suggest that formulated polyphenols primarily act by preventing oxidative damage, whereas the NR-induced increase in NAD^+ levels supports PARP1 (poly [ADP-ribose] polymerase 1)-mediated DNA repair [5,32]. However, the mechanisms underlying radiation-induced damage and its prevention may be more complex. For example, the cGAS-STING (cyclic GMP-AMP synthase-stimulator of interferon genes) pathway is activated by cytosolic DNA fragments, triggering the production of type I interferons and other inflammatory cytokines [33]. Reactive oxygen species (ROS) activate NF-κB, a key transcription factor in inflammation, promoting cytokine release [34,35]. Both DNA damage and ROS stimulate the assembly of inflammasomes, particularly NLRP3 (NOD-like receptor pyrin domain-containing protein 3) inflammasome, leading to activation of caspase-1 and the release of proinflammatory cytokines, which amplify inflammation and can contribute to radiation-induced tissue damage [36]. A cytokine storm might cause multi-organ failure in severe radiation exposure cases [37]. Radiation damages endothelial cells, increasing vascular permeability and pro-thrombotic responses, which results in inflammation, tissue hypoxia, and radiation-induced fibrosis over time [38]. Macrophages and neutrophils infiltrate damaged tissues, releasing additional ROS and cytokines [39]. Surviving cells may enter a senescence-associated secretory phenotype (SASP), continuously releasing pro-inflammatory factors such as IL-6, IL-8, and GM-CSF, contributing to chronic radiation-induced inflammation [40]. Moreover, in addition to cause direct cell death, radiation-induced DNA damage triggers p53 activation, which can promote different pro-apoptotic proteins [41]. Furthermore, cell damage-associated mitochondrial outer membrane permeabilization may favor the release to the cytosol of pro-apoptotic molecular signals [42]. Thus, in order to elucidate the mechanisms underlying the radioprotecting/radiomitigating effects described above, we first examined the expression of genes directly related to cell death, oxidative stress, inflammation and DNA repair. IEC were selected for these experiments, as IR is known to cause cellular damage and disruption of the epithelial barrier function [43]. Fig. 4A shows that immortalized IEC cultured *in vitro* were protected from IR-induced cell death following polyphenol treatment, and using concentrations and timing that mirror *in vivo* conditions. This protective effect was associated with reduced generation of ROS and maintenance of the mitochondrial membrane potential (MMP) at levels comparable to untreated controls (Fig. 4B). As shown in Fig. 4A, shRNAs were used to target mouse Nfe2l2 (which encodes Nrf2) or Nfkbie (which encodes the NF-KB Inhibitor Epsilon). Nfe2l2-shRNA significantly reduced the survival of immortalized IEC pretreated with polyphenols and exposed to X radiation. Thus, revealing a specific molecular pathway through which polyphenols exert their protective effects in irradiated cells.

As shown in Fig. 4C, and considering changes of at least a twofold increase or decrease relative to controls, *in vivo* administration of formulated polyphenols significantly increased the expression of anti-apoptotic markers bcl-2 and bcl-xl, while reducing the expression of pro-apoptotic markers bax and puma, compared to control IEC isolated from mice treated with vehicle. This expression pattern strongly supports an anti-apoptotic effect. Importantly, inhibition of intestinal epithelial apoptosis has been shown to improve survival in irradiated mice [44]. Consistent with these findings, polyphenol treatment also resulted in increased expression of sod1 and sod2, gpx (glutathione peroxidase) 2, txrnd (thioredoxin reductase) 1, sirt1 and sirt3, nrf2, and parp1 (twofold or more compared to controls), indicating potential antioxidant, anti-inflammatory, and pro-DNA repair effects (Fig. 4C). In this regard, it is worthy to mention that supplementation with NR, which supports NAD^+ and SIRT3-dependent deacetylation of SOD2 [45], may further decrease ROS generation and cell death.

As shown in Fig. 5A and B, changes in gene expression correlated to changes in protein levels (western blots). It is noteworthy the polyphenols-induced decrease in cMYC levels (Fig. 5A). For instance, it

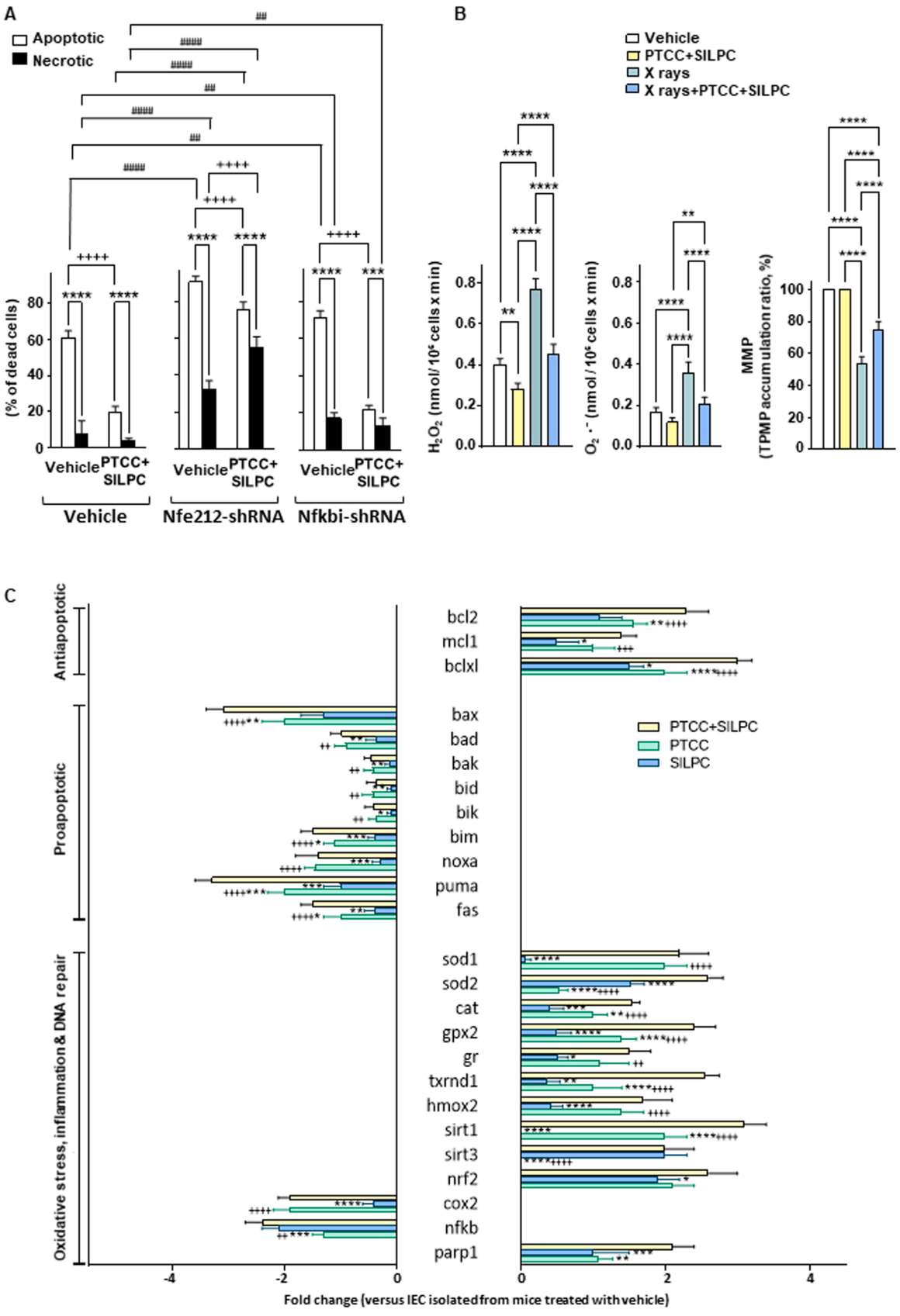

(caption on next page)

Fig. 4. Formulated polyphenols prevent radiation-induced cell death in intestinal epithelial cells. (**A**) X rays-induced IEC death. *In vitro* growing immortalized CI-muADINTESTI murine adult IEC were treated once per day with PTCC+SILPC x 5 days. Concentrations added to the cultures for PTCC and SILPC were half of the main peak measured in circulating blood (Fig. S4). Thereby, the effects induced by the *in vivo* treatment could be preserved under *in vitro* conditions. Cells received X radiation (7.2 Gy) at the end of day 5, as described under Methods. Cell death was analyzed 12 h after irradiation. Cells were transfected with specific shRNAs, 24 h before starting the 5-days treatment period. Data are shown as means ± SD of 5 independent experiments. Statistical analysis was performed using two-way ANOVA followed by Bonferroni's multiple comparisons test (***$P < 0.001$, ****$P < 0.0001$ comparing necrotic versus apoptotic cell death in each experimental group; $^{++++}P < 0.0001$ comparing *P*TCC+SILPC- versus vehicle-treated cells; $^{\#\#}P < 0.01$, $^{\#\#\#\#}P < 0.0001$ comparing cells treated with different shRNAs versus controls (vehicle). (**B**) ROS generation and MMP in immortalized IEC were also measured 12 h after irradiation. Data are presented as mean ± SD (n = 5 independent experiments per condition). Statistical significance was determined by one-way ANOVA followed by Bonferroni's post hoc test (**$P < 0.01$, ****$P < 0.0001$ for the indicated pairwise comparisons). (**C**) RT-PCR analysis of genes related to apoptosis, oxidative stress, inflammation and DNA repair in IEC isolated from mice right before irradiation and pretreated *in vivo* (as indicated in Fig. 1A) with vehicle or PTCC and/or SILPC. Data are mean ± SD (n = 4–5 mice per group). Statistical significance was assessed by one-way ANOVA followed by Bonferroni's multiple comparisons test (*$P < 0.05$, **$P < 0.01$, ***$P < 0.001$, ****$P < 0.0001$ comparing treatment with *P*TCC versus treatment with PTCC+SILPC; $^{++}P < 0.01$, $^{+++}P < 0.001$, $^{++++}P < 0.0001$ comparing treatment with SILPC versus treatment with PTCC+SILPC).

is known that SIRT1 (upregulated by polyphenols, Fig. 5A) directly interacts with cMYC, deacetylating it, thus promoting its proteasomal degradation [46]. Moreover, one way cMYC can induce apoptosis is by repressing anti-apoptotic Bcl-2 family proteins [47], an effect that is prevented by polyphenols (Fig. 5A). Polyphenol-induced decrease in cytosolic CytC (cytochrome C) and AIF (apoptosis-inducing factor) was associated with an increase in LC3-II (light chain 3-II) along with decrease of SQSTIM1 (sequestosome-1)/P62 levels (Fig. 5B), a strong indication that autophagy is induced. Autophagy helps to maintain homeostasis by removing damaged organelles and molecules, particularly under stress conditions such as IR exposure [48]. By promoting autophagy, cells can repair damage and survive rather than undergoing cell death [49]. As shown in Fig. 5C, using a cationic amphiphilic tracer dye that selectively labels autophagic vacuoles, we could visualize the polyphenol-induced increase in autophagy in isolated IEC from X rays-treated mice. Additionally, the attenuation of IR-induced elevations in plasma levels of multiple pro-inflammatory cytokines further supports the protective effects of polyphenols and NR treatment (Fig. 5D).

Our findings underscore the protective effects of formulated polyphenols and NR against radiation-induced damage, acting through multiple mechanisms. These compounds enhance cellular resilience to radiation by mitigating oxidative stress, cell death, and inflammation, while simultaneously promoting DNA repair and autophagy (Figs_4 and 5). Fig. 5E shows an integrated scheme illustrating how X-ray radiation disrupts cellular homeostasis and how combined PTCC, SILPC, and NR therapy intervenes.

3.5. Radioprotective and radiomitigative therapy and the efficacy of X rays in human triple-negative breast carcinoma and glioblastoma

To assess whether our formulation compromises the therapeutic efficacy of IR in different growing cancers, we utilized the MDA-MB-436 human triple-negative breast carcinoma (TNBC) and U87 glioblastoma (GB) models (ATCC, American Type Culture Collection). The highly aggressive BRCA1- and TP53-mutated, mesenchymal stem-like subtype, is typically responsive to radiotherapy [50]. On the other hand, GB shows intrinsic radioresistance and this characteristic can be even exacerbated in U87 by hypoxia via ROS-induced higher and long-term HIF-1 signal transduction activity [51].

Mice bearing orthotopic MDA-MB-436 or U87 MG-Luc2 tumors were treated with X-ray irradiation alone or in combination with PTCC, SILPC, NR, and CPT (PSNC, as depicted in Fig. 6). X-ray monotherapy drastically reduced MDA-MB-436 tumor growth, and co-treatment with PSNC did not attenuate this therapeutic effect (Fig. 6). Which indicates that PSNC does not compromise the radiation-induced effect on this TNBC model. On the other hand, the effect of X ray therapy on U87 was minimum. However, cotreatment with PSNC reduced U87 growth (Fig. 6), which suggests that the radioprotecting/radiomitigating formula may sensitize this GB model to radiation therapy.

To elucidate the mechanistic basis for these effects, in cancer cells isolated from the growing tumors, we investigated a) ROS generation, as cancer cells (including aggressive TNBC and GB) typically exhibit elevated basal ROS levels due to their high metabolic rate and oncogenic signaling, rendering them more vulnerable to additional ROS stress [52,53]; b) DNA damage and repair, given that cancer cells often harbor aberrant or less effective DNA repair pathways [53,54]. Furthermore, some flavonoids may bind and inhibit enzymes such as PARP1 in tumor cells, thus precluding an efficient repair of radiation-induced breaks [55]; c) NAD^+ levels, because if radiation triggers massive DNA damage in tumor cells, the NAD^+ may get quickly depleted, leading to energy crisis and cell death even in the presence of a NAD^+ booster [56]; d) tumor cell proliferation, VEGF and HIF-1α, since CPT may impair tumor growth and angiogenesis, potentially enhancing tumor radiosensitivity [57,58].

Polyphenols or PSNC treatment increased nuclear Nrf2 and its downstream antioxidant enzymes (e.g., SOD1, SOD2, and catalase) (Fig. 7A), leading to a reduction in total ROS (Fig. 7C). However, levels of hydrogen peroxide and superoxide remained significantly higher in MDA-MB-436 and U87 cells than in non-tumorigenic MCF-10A human mammary epithelial cells and SV40-immortalized human fetal glial cells (Fig. 7C), which indicates that cancer cells still remain under oxidative stress compared to their normal counterparts. Polyphenols or PSNC treatment also increased SIRT1 and SIRT3 levels (Fig. 7A), and NR supplementation elevated NAD^+ levels (Fig. 7B). Despite this, PARP1 levels were reduced in tumor cells following PSNC or polyphenol treatment (Fig. 7A), potentially limiting the DNA repair capacity of irradiated cancer cells. An effect which is the opposite of that observed in normal IEC (Fig. 5 A). For instance, a radiation-damage study in normal human keratinocytes demonstrated that resveratrol promotes PARP-1 activity (via tyrosyl-tRNA synthetase binding) to promote DNA repair [59]. This paradox may be explained if one takes into account that normal and cancer cells have fundamentally different redox states, signaling environments, and DNA damage levels. These differences may influence how polyphenols act. Furthermore, polyphenol treatment reduced Ki-67 immunostaining in tumor cells (Fig. 7D), indicating decreased proliferation. CPT additionally decreased HIF-1α and VEGF levels (Fig. 7D), which will pose a threat for cancer cell trying to adapt to low oxygen environments and to promote angiogenesis. Collectively, our data suggest that the PSNC formulation selectively protects non-tumor tissues while preserving the cytotoxic effects of radiation in cancer cells.

4. Discussion

Currently, available and proposed radioprotectors and radiomitigators exhibit limited efficacy in providing comprehensive protection against radiation-induced damage. Most of these compounds focus on specific tissues (e.g., bone marrow) rather than providing systemic protection, leaving critical organs like the gastrointestinal tract or the central nervous system vulnerable [60]. Additionally, while many radioprotective agents enhance acute survival by mitigating immediate radiation toxicity, they often do not prevent long-term complications,

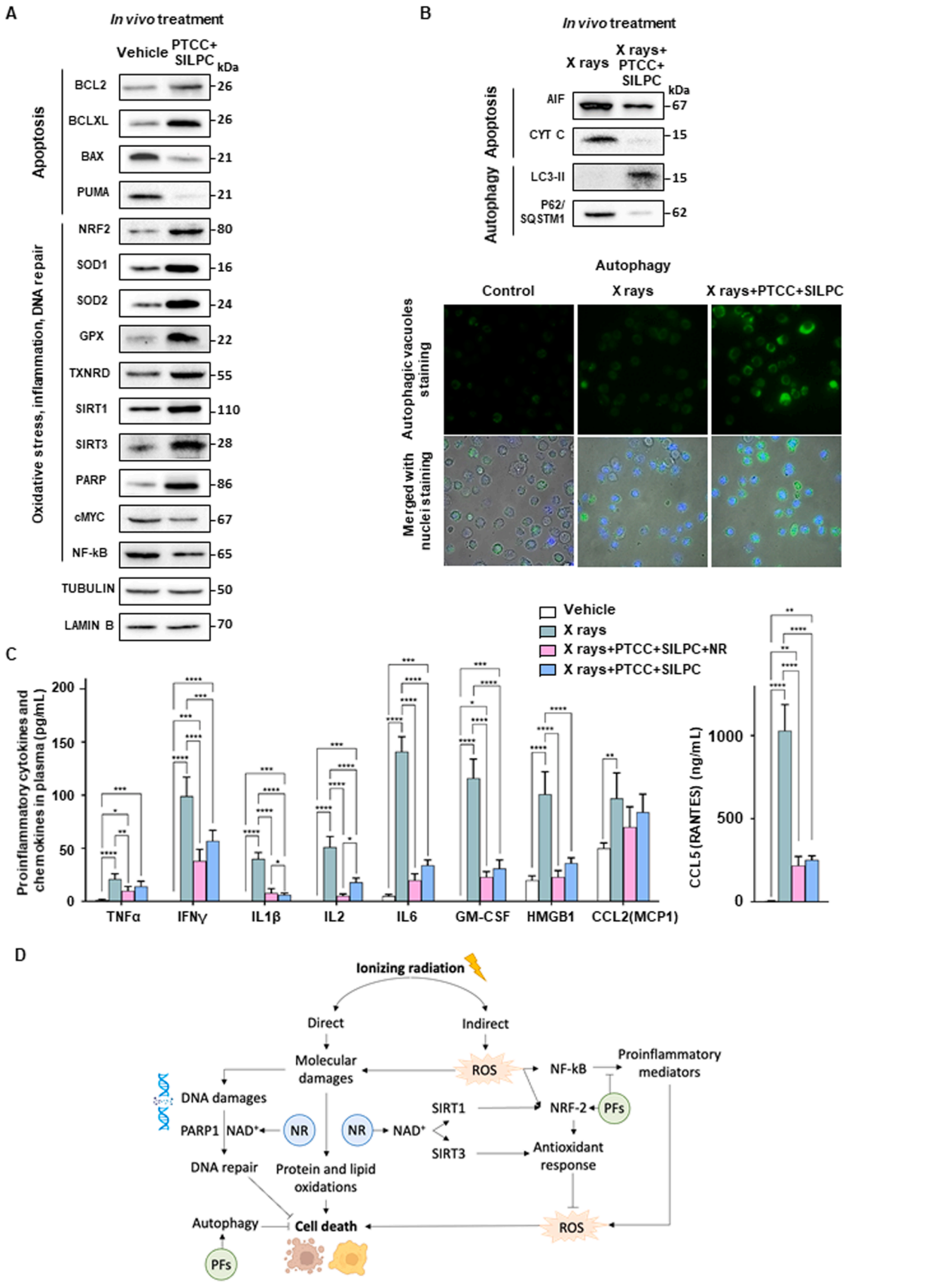

(caption on next page)

Fig. 5. Signaling mechanisms involved in the radioprotective effect of the combination of PTCC and SILPC. (**A**) Western blots to analyze proteins with expression levels that change at least twofold as compared to controls (Fig. 4C). p65NF-kB, NRF2, PARP1 and SIRT1 were analyzed in nuclear extracts, SOD2 and SIRT3 in mitochondrial extracts, and all other proteins in cell extracts. Protein extracts were obtained from IECs isolated from mice right before irradiation and pretreated with vehicle or PTCC and/or SILPC (Fig. 1A) (n = 4 different mice per experimental condition; see densitometric analysis in Fig. S5). (**B**) PTCC and SILPC treatment-induced autophagy. Western blots for AIF, CytC, LC3-II and p62/SQSTM1 (cell extracts). Protein extracts were obtained from IECs isolated from mice 12 h post-irradiation and pretreated with vehicle or PTCC and/or SILPC (Fig. 1 A) (n = 4 different mice per experimental condition; see densitometric analysis in Fig. S5). (**C**) Representative images showing labeled autophagic vacuoles (see under Methods) in IEC isolated from non-irradiated, irradiated, and irradiated mice treated with PTCC and SILPC (mice were treated as in Fig. 1A, and cells were isolated 5 days after irradiation). (**D**) Effect of PTCC, SILPC, and NR treatment on plasma proinflammatory cytokine levels in mice exposed to X-Rays. Mice were treated as in Fig. 1D and IEC were isolated 5 days after the irradiation. Data are shown as mean ± SD (n = 5 per group). Statistical significance was assessed by one-way ANOVA followed by Bonferroni's multiple comparisons test (*$P < 0.05$, **$P < 0.01$, ***$P < 0.001$, ****$P < 0.0001$). (**E**) Schematic representation of the molecular mechanisms eliciting cell survival after irradiation. PFs, polyphenols (PTCC and SILPC).

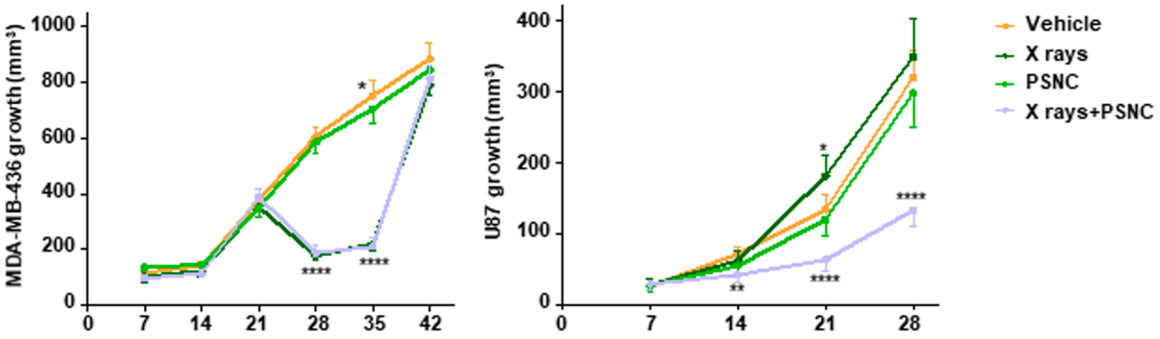

Fig. 6. Effect of PTCC, SILPC, NR, CPT and/or X-ray treatment on growing human TNBC and GB. Growth of MDA-MB-436 carcinoma and U-87 GB orthotopically inoculated in mice. Tumors were irradiated with X-rays targeted specifically to the tumor site using a linear accelerator (see under Methods), with surrounding tissue shielded. A total radiation dose of 20 Gy [78,79] was administered using a clinically relevant schedule: for MDA-MB-436 tumors, 10 Gy per fraction were delivered on days 21 and 28 after tumor inoculation; for U87 tumors, 2 Gy per fraction were given daily over 10 consecutive days, from day 7 to day 16 post-inoculation. Drug administration followed the same protocol as in previous experiments (see Fig. 1D), beginning five days before the first administration of X rays. Data are mean ± SD (MDA-MB-436, n = 10 mice per experimental group; U87, n = 7 mice per experimental group). Statistical significance over time was assessed by two-way repeated measures ANOVA with Bonferroni's post hoc tests comparing each treatment group versus vehicle (*$P < 0.05$, **$P < 0.01$, ****$P < 0.0001$).

including radiation-induced fibrosis, chronic inflammation, and progressive organ dysfunction [61]. Such delayed effects are particularly concerning in scenarios involving partial-body or whole-body radiation exposure, where late-onset pathologies can severely impair quality of life. Moreover, the FDA-approved radioprotector, amifostine, has shown significant adverse effects, i.e., hypotension, nausea, and vomiting, which limit its tolerability at therapeutic doses [62]. A similar scenario is found with the FDA-approved radiomitigators, where common side effects for G-CSF and GM-CSF include bone and muscle pain, headache, and fatigue. GM-CSF may also cause fever, diarrhea, nausea, skin rash, and vomiting, while TPO-RAs can cause rebound thrombocytopenia [63]. This has spurred research into alternative compounds, such as mitochondrial-targeted antioxidants (e.g., MnSOD mimetics such as M40403) [64] or toll-like receptor modulators (e.g., the TLR2/6 ligand FSL1 lipopeptide) [65], which may offer improved systemic protection with fewer side effects.

Despite these advances, ideal radioprotectors and/or radiomitigators that may provide broad-spectrum protection against acute and chronic radiation effects, while maintaining an acceptable safety profile have remained elusive. Our present study investigates an innovative and fully oral formulation that combines PTCC and SILPC as radioprotectors, alongside NR and CPT as radiomitigators. This staged regimen aligns with established definitions distinguishing radioprotectors (given before exposure) from mitigators (given after exposure but prior to full clinical expression). By pairing time-sensitive agents intended to blunt early oxidative/inflammatory injury with post-exposure mitigators designed to support recovery pathways during the subacute phase, our approach addresses the fact that radiation injury evolves over time and across multiple organ systems. Benefits of an oral approach over injectable alternatives imply, e.g., ease of administration and potential for emergency use. Specifically, oral administration was prioritized to enable rapid, scalable distribution and self-administration, which is critical when parenteral therapies, laboratory monitoring, and hospital-level supportive care may be constrained. In humans, germ-free isolation -often used in rodent studies- is not operationally realistic at the population scale. However, the clinical analogue of rodent supportive care is infection risk mitigation and treatment, including protective isolation precautions when feasible, early recognition and management of infection, and hematopoietic support measures such as myeloid cytokines for patients with myelosuppressive exposures, as recommended in clinical guidance for ARS. In mass-casualty settings, triage-based deployment and resource-dependent scaling of supportive care are expected; thus, an oral countermeasure could serve as a bridge and adjunct rather than a substitute for indicated clinical management. Our multifaceted approach enhances survival in irradiated mice (Fig. 1E) by reducing oxidative damages (Fig. 2A-C) and cytogenetic damages (Fig. 2D-H), promoting DNA recovery (Fig. 3B), and facilitating hematopoietic, intestinal and neuromotor activity recovery (Fig. 3C-F). Furthermore, mechanistic studies in radiation-sensitive intestinal cells reveal that the formulation activates the Nrf2-dependent antioxidant response, reduces NF-kB-driven inflammation, prevents cell death, and induces autophagy (Figs. 4 and 5).

PTCC is a formulation of the nutraceutical PT, which enhances its oral bioavailability in rats by tenfold [6]. SILPC combines the flavonoid, the most active in milk thistle, with phosphatidylcholine to form a phytosome complex that also enhances SIL bioavailability [7]. NR is a water-soluble derivative of vitamin B3 that serves as a more efficient precursor to NAD^+ than niacin or nicotinamide, with fewer side effects. Inside cells, NR is converted to NMN and then to NAD^+. However, in the extracellular space, NMN must first be converted back to NR to cross the plasma membrane, making NR a more efficient NAD^+ precursor [66,67]. CPT, if given chronically at high doses, has potential side effects i.e.,

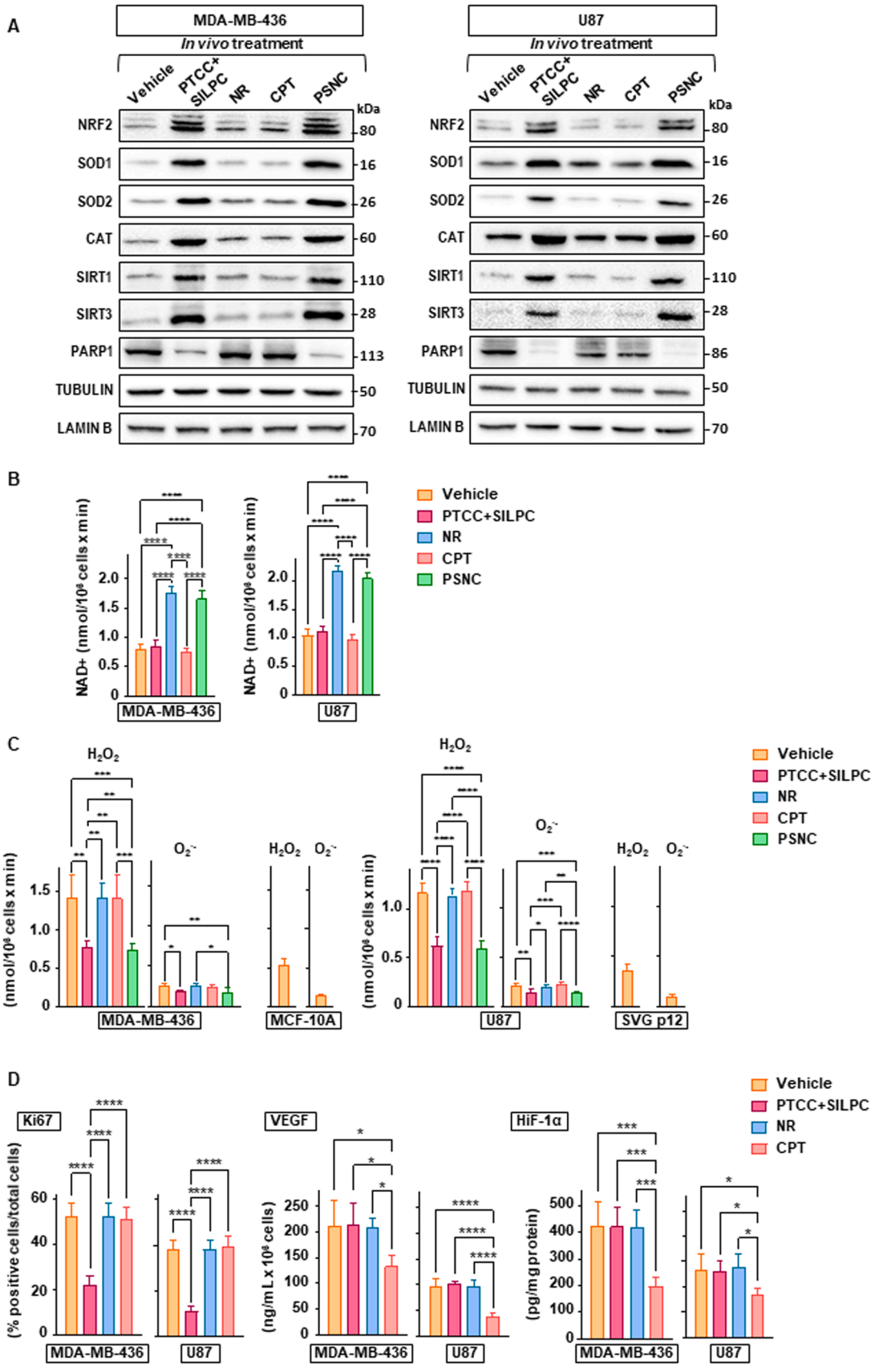

(caption on next page)

Fig. 7. Molecular mechanisms involved in the effect of the radioprotective/radiomitigating formula in cancer cells. (**A**) Western blot analysis of nuclear Nrf2, SIRT1, and PARP1; cytosolic SOD1, and CAT; and mitochondrial SOD2 and SIRT3 levels in isolated MDA-MB-436 and U87 cells from *in vivo* growing tumors (n = 4 per tumor and experimental group; see densitometric analysis in Fig. S6). In both cases and before isolation of the tumor cells, mice were treated for 10 days with the different compounds, starting two weeks after tumor inoculation. (**B**) NAD^+ levels and (**C**) ROS generation in MDA-MB-436, MCF-10A, U87 and SVG p12 cells. Cancer cells were isolated as described under Methods. Data are mean ± SD of n = 5 biologically independent tumors per cancer cell line and n = 5 independent cultures per non-tumor cell line. Statistical significance was determined by one-way ANOVA with Bonferroni's post hoc test (*$P < 0.05$, **$P < 0.01$, ***$P < 0.001$, ****$P < 0.0001$). (**D**) Ki67, VEFG and HIF-1α levels (ELISA). In MDA-MB-436 and U87 cells, isolated from the growing tumors, Ki67 was measured by immunohistochemistry; whereas VEGF and HIF-1α were measured by ELISA in the extracellular medium or the cell lysate, respectively (see Methods). Mice were treated and tumor cells isolated as in (A). Data are means ± SD (n = 5 per group). Statistical significance was determined by one-way ANOVA with Bonferroni's post hoc test (*$P < 0.05$; ***$P < 0.001$; ****$P < 0.0001$).

cough, increase in the plasma levels of bradykinin, angioedema, agranulocytosis, proteinuria, hyperkalemia, taste alteration, itching, teratogenicity, postural hypotension, acute renal failure, and leukopenia [68]. Nevertheless, none of the compounds present in the radioprotecting/radiomitigating formula, at the doses and treatment regime proposed, exert any significant toxicity per se (see Table S1). Importantly, the ingredients of this formulation have been approved for human use, either as nutritional supplements (PTCC, SILPC, NR) or as a drug (CPT) [see e.g., at (www.fda.gov)], and can be stored in a compact, long-lasting form that requires minimal space. Despite these considerations, potential future applications in humans will have to evaluate (a) pharmacokinetics and safety, (b) dose optimization and long-term effects, particularly in cases of repeated exposures to irradiation, (c) efficacy in other animal species and settings, and (d) the limitations of a pre-irradiation treatment using a combination of polyphenols. Additionally, to increase operational practicality, future studies should test simplified regimens, such as (i) fully post-exposure initiation without any pre-exposure dosing and (ii) shorter treatment durations, while aiming to maintain efficacy on survival and key mechanistic endpoints.

Furthermore, the proposed formulation may protect normal tissues without shielding cancer cells from radiation-induced killing (Figs. 6 and 7). One of the core findings is the differential modulation of ROS in tumor versus normal cells. While PSNC treatment increased nuclear Nrf2 and antioxidant enzymes (SOD1, SOD2, catalase) (Fig. 7A), ROS levels remained significantly higher in MDA-MB-436 and U87 cells compared to non-tumorigenic breast epithelial and glial cells (Fig. 7C). Cancer cells operate under elevated basal ROS levels due to high metabolic activity and oncogenic signaling, making them more susceptible to oxidative insults even after antioxidant intervention [69].

Another critical insight lies in PSNC's impact on NAD^+ metabolism and DNA repair. PSNC treatment increased intracellular NAD^+ and levels of SIRT1 and SIRT3 (Figs_ 5A and 7A), deacetylases involved in DNA repair, stress resistance, and mitochondrial function [70]. However, paradoxically, tumor cells treated with PSNC exhibited decreased PARP1 levels (Fig. 7A), a major NAD^+-consuming enzyme essential for DNA damage repair. In fact, PARP1 inhibition has been widely studied as a method to sensitize tumors to IR by preventing efficient repair of radiation-induced DNA strand breaks [71]. In this regard, it has been shown that e.g., resveratrol can improve the efficiency of DNA repair, particularly double-strand break repair, and reduce replicative stress after exposure to chemical or IR damage [72]. In stark contrast, resveratrol can act as a pro-oxidant in the tumor microenvironment, promoting DNA damage and activating damage signaling pathways in various cancer cell types. This pro-oxidant effect, particularly in the presence of copper ions, can lead to DNA breaks and the formation of γ-H2AX foci, which are indicative of DNA damage [55]. Notably, head and neck carcinoma and breast cancer cells incurred more DNA damage from resveratrol than their normal cell counterparts. In addition, as another example, gemcitabine-resistant pancreatic carcinoma cells were found to have upregulated c-Met (a survival signaling kinase) and PARP1, which may contribute to their chemoresistance. Resveratrol treatment inhibited the expression of both c-Met and PARP1 in these resistant cancer cells [73]. The dual modulation -increasing NAD^+ but lowering PARP1 (likely linked to the harsher oxidative environment)- may deprive tumor cells of an effective DNA repair response, rendering them more susceptible to radiation-induced cytotoxicity, while preserving DNA repair capacity in non-tumor tissues.

Furthermore, PSNC inhibited tumor proliferation and angiogenic potential. Reduced Ki-67 levels indicates suppression of proliferative capacity in both tumor models (Fig. 7D). CPT contributed additional antitumor activity by decreasing HIF-1α and VEGF levels (Fig. 7D), key mediators of hypoxia adaptation and neovascularization [74,75]. HIF-1α is known to confer radioresistance by promoting cell survival, metabolic reprogramming, and angiogenesis under hypoxic conditions [76]. By downregulating this pathway, PSNC may abrogate hypoxia-induced tumor resilience and further enhance radiosensitivity in GB. The radiosensitizing effect of PSNC in U87 cells, a model for highly radioresistant GB, is particularly promising. GB typically resists radiotherapy due to enhanced DNA repair capacity and a hypoxic microenvironment that supports survival via HIF-1α signaling [77]. PSNC appears to counteract both mechanisms (Fig. 7D). The potential application of PSNC in other radioresistant tumors -such as pancreatic, head and neck, and hypoxic prostate cancers- warrants further exploration. Therefore, normal and cancer cells respond differently to IR when treated with a radioprotecting/radiomitigating formula due to their inherent biological characteristics. Normal cells are flexible; they can activate antioxidant responses, efficiently repair DNA, and pause their growth to recover from damage. In contrast, cancer cells are chronically stressed due to oncogene activation, rapid proliferation and abnormal mitochondrial metabolism, relying on fragile survival mechanisms. Translationally, our findings represent a clear clinical advantage since a) higher radiation doses could be safely delivered to tumors, b) treatment-related side effects could be significantly reduced, and c) the therapeutic index (the ratio of tumor control to normal tissue damage) should improve.

In conclusion, this study demonstrates that the combined administration of PTCC, SILPC, NR, and CPT provides robust radioprotection and radiomitigation, significantly improving both short-term and long-term survival after whole-body irradiation. The formulation mitigates oxidative damage, enhances DNA repair, and promotes recovery across multiple organ systems through Nrf2 activation, NF-kB suppression, cell death inhibition and autophagy induction. Importantly, the regimen preserved radiation-induced tumor control in triple-negative breast cancer and even sensitized radioresistant glioblastoma, via persistent oxidative stress, reduced PARP1 expression, and inhibition of HIF-1α and VEGF signaling.

5. Conclusion

Together, these results identify a fully oral medical countermeasure with substantial translational potential for radiotherapy, pre-irradiation exposure, spaceflight, or military preparedness. Further studies are warranted to optimize dosing strategies and evaluate safety, pharmacokinetics, and efficacy in humans.

Compliance with ethics requirements

This study was performed in accordance with ethical standards, according to the Declaration of Helsinki, and according to national and international guidelines. The ethics committee in animal

experimentation of the University and Polytechnic Hospital La Fe (Valencia, Spain) approved the study.

CRediT authorship contribution statement

Juan I. Villaescusa: Investigation. **Paz Moreno-Murciano:** Investigation. **María Benlloch:** Investigation. **María Oriol-Caballo:** Investigation, Formal analysis, Data curation. **Rosario Salvador-Palmer:** Writing – review & editing, Validation, Software, Investigation, Formal analysis. **Elena Obrador:** Writing – review & editing, Writing – original draft, Visualization, Project administration, Investigation, Funding acquisition, Conceptualization. **Rafael López-Blanch:** Validation, Investigation, Formal analysis, Data curation. **Joan Albertí:** Investigation, Formal analysis. **José M. Estrela:** Writing – review & editing, Writing – original draft, Visualization, Supervision, Investigation, Funding acquisition, Conceptualization. **Alegría Montoro:** Investigation. **Rafel Prohens:** Investigation, Formal analysis.

Funding and acknowledgements

This work was funded by MCIN/AEI/10.13039/501100011033 and European Union Next Generation EU/PRTR [grant number CPP2021–8817] and MICIU/AEI/10.13039/501100011033 and FEDER, UE [grant number PID2023–146158OB-I00]. We thank Drs. Viviana Velasco and Delia Castellano for their technical assistance with animal experiments, and Dr. José Perez-Calatayud for his help and scientific advice with the linear accelerator.

Declaration of Competing Interest

J.M.E. currently receives personal consulting fees from Circe Health Science, Spain. E.O. and J.M.E. are stockholders in Scientia BioTech, Spain. R.P. and J.A. are stockholders in Circe Health Science. R.L.B., M. O.C., R.S.P., P.M.M., V.R.D., M.B., J.I.V. and A.M declare no competing interests.

Appendix A. Supporting information

Supplementary data associated with this article can be found in the online version at doi:10.1016/j.biopha.2026.119323.

Data Availability

All data are available through a figshare link

References

[1] N. Dainiak, J. Albanese, Medical management of acute radiation syndrome, J. Radiol. Prot. 42 (2022) 031002, https://doi.org/10.1088/1361-6498/ac7d18.
[2] L. Barazzuol, R.P. Coppes, P. van Luijk, Prevention and treatment of radiotherapy-induced side effects, Mol. Oncol. 14 (2020) 1538–1554, https://doi.org/10.1002/1878-0261.12750.
[3] S.K. Shakyawar, N.K. Mishra, N.N. Vellichirammal, L. Cary, T. Helikar, R. Powers, R.E. Oberley-Deegan, D.B. Berkowitz, K.W. Bayles, V.K. Singh, C. Guda, A review of radiation-induced alterations of multi-omic profiles, radiation injury biomarkers, and countermeasures, Radiat. Res 199 (2023) 89–111, https://doi.org/10.1667/RADE-21-00187.1.
[4] V.K. Singh, T.M. Seed, Radiation countermeasures for hematopoietic acute radiation syndrome: growth factors, cytokines and beyond, Int J. Radiat. Biol. 97 (2021) 1526–1547, https://doi.org/10.1080/09553002.2021.1969054.
[5] E. Obrador, R. Salvador-Palmer, B. Pellicer, R. López-Blanch, J.A. Sirerol, J. I. Villaescusa, A. Montoro, R.W. Dellinger, J.M. Estrela, Combination of natural polyphenols with a precursor of NAD+ and a TLR2/6 ligand lipopeptide protects mice against lethal γ radiation, J. Adv. Res 45 (2023) 73–86, https://doi.org/10.1016/j.jare.2022.05.005.
[6] L. Bofill, R. Barbas, D. de Sande, M. Font-Bardia, C. Ràfols, J. Albertí, R. Prohens, A novel, extremely bioavailable cocrystal of pterostilbene, Cryst. Growth & Des. 21 (2021) 2315–2323, https://doi.org/10.1021/acs.cgd.0c01716.
[7] P. Kidd, K. Head, A review of the bioavailability and clinical efficacy of milk thistle phytosome: a silybin-phosphatidylcholine complex (Siliphos), Alter. Med Rev. 10 (2005) 193–203.
[8] S.A.J. Trammell, M.S. Schmidt, B.J. Weidemann, P. Redpath, F. Jaksch, R. W. Dellinger, Z. Li, E.D. Abel, M.E. Migaud, C. Brenner, Nicotinamide riboside is uniquely and orally bioavailable in mice and humans, Nat. Commun. 7 (2016) 12948, https://doi.org/10.1038/ncomms12948.
[9] E.A. McCart, Y.H. Lee, J. Jha, O. Mungunsukh, W.B. Rittase, T.A. Summers, J. Muir, R.M. Day, Delayed captopril administration mitigates hematopoietic injury in a murine model of total body irradiation, Sci. Rep. 9 (2019) 2198, https://doi.org/10.1038/s41598-019-38651-2.
[10] O. Mungunsukh, J. George, E.A. McCart, A.L. Snow, J.J. Mattapallil, S.R. Mog, R.A. M. Panganiban, D.L. Bolduc, W.B. Rittase, R.M. Bouten, R.M. Day, Captopril reduces lung inflammation and accelerated senescence in response to thoracic radiation in mice, J. Radiat. Res. 62 (2021) 236–248, https://doi.org/10.1093/jrr/rraa142.
[11] S.J. Van Der Veen, G. Ghobadi, R.A. De Boer, H. Faber, M.V. Cannon, P.W. Nagle, S. Brandenburg, J.A. Langendijk, P. Van Luijk, R.P. Coppes, ACE inhibition attenuates radiation-induced cardiopulmonary damage, Radiother. Oncol. 114 (2015) 96–103, https://doi.org/10.1016/j.radonc.2014.11.017.
[12] J.E. Moulder, E.P. Cohen, B.L. Fish, Captopril and losartan for mitigation of renal injury caused by single-dose total-body irradiation, Radiat. Res 175 (2011) 29–36, https://doi.org/10.1667/RR2400.1.
[13] W. Stern, P. Alaei, R. Berbeco, L.A. DeWerd, J. Kamen, C. MacKenzie, E.G. Moros, Y. Poirier, C.A. Potter, D. Schaue, I.S. Patallo, M. Abend, S. Swarts, F. Trompier, Recommendations for harmonized reporting of radiation dosimetry by adoption of compatibility in irradiation research protocols expert roundtable (CIRPER), Int. J. Radiat. Biol. 100 (2024) 821–823, https://doi.org/10.1080/09553002.2024.2331130.
[14] E. Obrador, R. Salvador, P. Marchio, R. López-Blanch, A. Jihad-Jebbar, P. Rivera, S. L. Vallés, S. Banacloche, J. Alcácer, N. Colomer, J.A. Coronado, S. Alandes, E. Drehmer, M. Benlloch, J.M. Estrela, Nicotinamide riboside and pterostilbene cooperatively delay motor neuron failure in ALS SOD1G93A Mice, Mol. Neurobiol. 58 (2021) 1345–1371, https://doi.org/10.1007/s12035-020-02188-7.
[15] D.B. Morton, P.H. Griffiths, Guidelines on the recognition of pain, distress and discomfort in experimental animals and an hypothesis for assessment, Vet. Rec. 116 (1985) 431–436, https://doi.org/10.1136/vr.116.16.431.
[16] J. Yoshino, S.-I. Imai, Accurate measurement of nicotinamide adenine dinucleotide (NAD^+) with high-performance liquid chromatography, Methods Mol. Biol. 1077 (2013) 203–215, https://doi.org/10.1007/978-1-62703-637-5_14.
[17] P.F. Crain, Preparation and enzymatic hydrolysis of DNA and RNA for mass spectrometry, Methods Enzym. 193 (1990) 782–790, https://doi.org/10.1016/0076-6879(90)93450-y.
[18] R. M'kacher, E. El Maalouf, G. Terzoudi, M. Ricoul, L. Heidingsfelder, I. Karachristou, E. Laplagne, W.M. Hempel, B. Colicchio, A. Dieterlen, G. Pantelias, L. Sabatier, Detection and automated scoring of dicentric chromosomes in nonstimulated lymphocyte prematurely condensed chromosomes after telomere and centromere staining, Int J. Radiat. Oncol. Biol. Phys. 91 (2015) 640–649, https://doi.org/10.1016/j.ijrobp.2014.10.048.
[19] G.E. Pantelias, H.D. Maillie, A simple method for premature chromosome condensation induction in primary human and rodent cells using polyethylene glycol, Somat. Cell Genet 9 (1983) 533–547, https://doi.org/10.1007/BF01574257.
[20] W. Schmid, The micronucleus test, Mutat. Res 31 (1975) 9–15, https://doi.org/10.1016/0165-1161(75)90058-8.
[21] M.N. Berry, D.S. Friend, High-yield preparation of isolated rat liver parenchymal cells: a biochemical and fine structural study, J. Cell Biol. 43 (1969) 506–520, https://doi.org/10.1083/jcb.43.3.506.
[22] C.L. Graves, S.W. Harden, M. LaPato, M. Nelson, B. Amador, H. Sorenson, C. J. Frazier, S.M. Wallet, A method for high purity intestinal epithelial cell culture from adult human and murine tissues for the investigation of innate immune function, J. Immunol. Methods 414 (2014) 20–31, https://doi.org/10.1016/j.jim.2014.08.002.
[23] G.J. Brewer, J.R. Torricelli, Isolation and culture of adult neurons and neurospheres, Nat. Protoc. 2 (2007) 1490–1498, https://doi.org/10.1038/nprot.2007.207.
[24] C.E. Wiedmeyer, D. Ruben, C. Franklin, Complete blood count, clinical chemistry, and serology profile by using a single tube of whole blood from mice, J. Am. Assoc. Lab Anim. Sci. 46 (2007) 59–64.
[25] P. Lundberg, R. Skoda, Hematology testing in mice, Curr. Protoc. Mouse Biol. 1 (2011) 323–346, https://doi.org/10.1002/9780470942390.mo110088.
[26] M.M. Bradford, A rapid and sensitive method for the quantitation of microgram quantities of protein utilizing the principle of protein-dye binding, Anal. Biochem. 72 (1976) 248–254, https://doi.org/10.1016/0003-2697(76)90527-3.
[27] C. Weidensteiner, W. Reichardt, P.J. Shami, J.E. Saavedra, L.K. Keefer, B. Baumer, A. Werres, R. Jasinski, N. Osterberg, A. Weyerbrock, Effects of the nitric oxide donor JS-K on the blood-tumor barrier and on orthotopic U87 rat gliomas assessed by MRI, Nitric Oxide 30 (2013) 17–25, https://doi.org/10.1016/j.niox.2013.01.003.
[28] M. Benlloch, E. Obrador, S.L. Valles, M.L. Rodriguez, J.A. Sirerol, J. Alcácer, J. A. Pellicer, R. Salvador, C. Cerdá, G.T. Sáez, J.M. Estrela, Pterostilbene Decreases the Antioxidant Defenses of Aggressive Cancer Cells In Vivo: A Physiological Glucocorticoids- and Nrf2-Dependent Mechanism, Antioxid. Redox Signal 24 (2016) 974–990, https://doi.org/10.1089/ars.2015.6437.
[29] Y. Zhang, M. Dai, Z. Yuan, Methods for the detection of reactive oxygen species, Anal. Methods 10 (2018) 4625–4638, https://doi.org/10.1039/C8AY01339J.
[30] J.L. Scarlett, P.W. Sheard, G. Hughes, E.C. Ledgerwood, H.H. Ku, M.P. Murphy, Changes in mitochondrial membrane potential during staurosporine-induced

apoptosis in Jurkat cells, FEBS Lett. 475 (2000) 267–272, https://doi.org/10.1016/s0014-5793(00)01681-1.
[31] A.M. James, Y.H. Wei, C.Y. Pang, M.P. Murphy, Altered mitochondrial function in fibroblasts containing MELAS or MERRF mitochondrial DNA mutations, Biochem J. 318 (Pt 2) (1996) 401–407, https://doi.org/10.1042/bj3180401.
[32] A. Bürkle, Poly(APD-ribosyl)ation, a DNA damage-driven protein modification and regulator of genomic instability, Cancer Lett. 163 (2001) 1–5, https://doi.org/10.1016/s0304-3835(00)00694-7.
[33] Q. Chen, L. Sun, Z.J. Chen, Regulation and function of the cGAS-STING pathway of cytosolic DNA sensing, Nat. Immunol. 17 (2016) 1142–1149, https://doi.org/10.1038/ni.3558.
[34] M.J. Morgan, Z. Liu, Crosstalk of reactive oxygen species and NF-κB signaling, Cell Res 21 (2011) 103–115, https://doi.org/10.1038/cr.2010.178.
[35] T. Liu, L. Zhang, D. Joo, S.-C. Sun, NF-κB signaling in inflammation, Signal Transduct. Target Ther. 2 (2017) 17023, https://doi.org/10.1038/sigtrans.2017.23.
[36] B.K. Ziehr, J.A. MacDonald, Regulation of NLRPs by reactive oxygen species: A story of crosstalk, Biochim Biophys. Acta Mol. Cell Res 1871 (2024) 119823, https://doi.org/10.1016/j.bbamcr.2024.119823.
[37] J.G. Kiang, A.O. Olabisi, Radiation: a poly-traumatic hit leading to multi-organ injury, Cell Biosci. 9 (2019) 25, https://doi.org/10.1186/s13578-019-0286-y.
[38] B. Baselet, P. Sonveaux, S. Baatout, A. Aerts, Pathological effects of ionizing radiation: endothelial activation and dysfunction, Cell Mol. Life Sci. 76 (2018) 699–728, https://doi.org/10.1007/s00018-018-2956-z.
[39] E. Kolaczkowska, P. Kubes, Neutrophil recruitment and function in health and inflammation, Nat. Rev. Immunol. 13 (2013) 159–175, https://doi.org/10.1038/nri3399.
[40] Z. Ungvari, A. Podlutsky, D. Sosnowska, Z. Tucsek, P. Toth, F. Deak, T. Gautam, A. Csiszar, W.E. Sonntag, Ionizing radiation promotes the acquisition of a senescence-associated secretory phenotype and impairs angiogenic capacity in cerebromicrovascular endothelial cells: role of increased dna damage and decreased DNA repair capacity in microvascular radiosensitivity, J. Gerontol. A Biol. Sci. Med Sci. 68 (2013) 1443–1457, https://doi.org/10.1093/gerona/glt057.
[41] K. Nakano, K.H. Vousden, PUMA, a novel proapoptotic gene, is induced by p53, Mol. Cell 7 (2001) 683–694, https://doi.org/10.1016/s1097-2765(01)00214-3.
[42] J. Mi, E. Bolesta, D.L. Brautigan, J.M. Larner, PP2A regulates ionizing radiation-induced apoptosis through Ser46 phosphorylation of p53, Mol. Cancer Ther. 8 (2009) 135–140, https://doi.org/10.1158/1535-7163.MCT-08-0457.
[43] E.J. Orzechowska-Licari, J.F. LaComb, M. Giarrizzo, V.W. Yang, A.B. Bialkowska, Intestinal Epithelial Regeneration in Response to Ionizing Irradiation, J. Vis. Exp. (2022), https://doi.org/10.3791/64028.
[44] E. Jung, E.E. Perrone, P. Brahmamdan, J.S. McDonough, A.M. Leathersich, J. A. Dominguez, A.T. Clark, A.C. Fox, W.M. Dunne, R.S. Hotchkiss, C. M. Coopersmith, Inhibition of intestinal epithelial apoptosis improves survival in a murine model of radiation combined injury, PloS One 8 (2013) e77203, https://doi.org/10.1371/journal.pone.0077203.
[45] Y. Chen, J. Zhang, Y. Lin, Q. Lei, K.-L. Guan, S. Zhao, Y. Xiong, Tumour suppressor SIRT3 deacetylates and activates manganese superoxide dismutase to scavenge ROS, EMBO Rep. 12 (2011) 534–541, https://doi.org/10.1038/embor.2011.65.
[46] K.-S. Hong, J.-I. Park, M.-J. Kim, H.-B. Kim, J.-W. Lee, T.T. Dao, W.K. Oh, C.-D. Kang, S.-H. Kim, Involvement of SIRT1 in hypoxic down-regulation of c-Myc and β-catenin and hypoxic preconditioning effect of polyphenols, Toxicol. Appl. Pharm. 259 (2012) 210–218, https://doi.org/10.1016/j.taap.2011.12.025.
[47] C.M. Eischen, D. Woo, M.F. Roussel, J.L. Cleveland, Apoptosis triggered by Myc-induced suppression of Bcl-X(L) or Bcl-2 is bypassed during lymphomagenesis, Mol. Cell Biol. 21 (2001) 5063–5070, https://doi.org/10.1128/MCB.21.15.5063-5070.2001.
[48] E.G. Foerster, T. Mukherjee, L. Cabral-Fernandes, J.D.B. Rocha, S.E. Girardin, D. J. Philpott, How autophagy controls the intestinal epithelial barrier, Autophagy 18 (2022) 86–103, https://doi.org/10.1080/15548627.2021.1909406.
[49] H. Qin, H. Zhang, X. Zhang, S. Zhang, S. Zhu, H. Wang, Resveratrol protects intestinal epithelial cells against radiation-induced damage by promoting autophagy and inhibiting apoptosis through SIRT1 activation, J. Radiat. Res 62 (2021) 574–581, https://doi.org/10.1093/jrr/rrab035.
[50] N. Xiong, H. Wu, Z. Yu, Advancements and challenges in triple-negative breast cancer: a comprehensive review of therapeutic and diagnostic strategies, Front Oncol. 14 (2024) 1405491, https://doi.org/10.3389/fonc.2024.1405491.
[51] C.-H. Hsieh, C.-H. Lee, J.-A. Liang, C.-Y. Yu, W.-C. Shyu, Cycling hypoxia increases U87 glioma cell radioresistance via ROS induced higher and long-term HIF-1 signal transduction activity, Oncol. Rep. 24 (2010) 1629–1636, https://doi.org/10.3892/or_00001027.
[52] B.A. Humphries, A. Zhang, J.M. Buschhaus, A. Bevoor, A. Farfel, S. Rajendran, A. C. Cutter, G.D. Luker, Enhanced mitochondrial fission inhibits triple-negative breast cancer cell migration through an ROS-dependent mechanism, iScience 26 (2023) 106788, https://doi.org/10.1016/j.isci.2023.106788.
[53] C. Olivier, L. Oliver, L. Lalier, F.M. Vallette, Drug resistance in glioblastoma: the two faces of oxidative stress, Front Mol. Biosci. 7 (2020) 620677, https://doi.org/10.3389/fmolb.2020.620677.
[54] J.L. Hopkins, L. Lan, L. Zou, DNA repair defects in cancer and therapeutic opportunities, Genes Dev. 36 (2022) 278–293, https://doi.org/10.1101/gad.349431.122.
[55] F.A. Lagunas-Rangel, R.M. Bermúdez-Cruz, Natural compounds that target dna repair pathways and their therapeutic potential to counteract cancer cells, Front Oncol. 10 (2020) 598174, https://doi.org/10.3389/fonc.2020.598174.
[56] W.L. Santivasi, F. Xia, Ionizing radiation-induced DNA damage, response, and repair, Antioxid. Redox Signal 21 (2014) 251–259, https://doi.org/10.1089/ars.2013.5668.
[57] S. Attoub, A.M. Gaben, S. Al-Salam, M. a H. Al Sultan, A. John, M.G. Nicholls, J. Mester, G. Petroianu, Captopril as a potential inhibitor of lung tumor growth and metastasis, Ann. N. Y Acad. Sci. 1138 (2008) 65–72, https://doi.org/10.1196/annals.1414.011.
[58] W.K. Cho, S.-W. Shin, S.-Y. Kim, C.-W. Hong, C. Choi, W. Park, J.M. Noh, Immunomodulatory effect of captopril and local irradiation on myeloid-derived suppressor cells, Radiat. Oncol. J. 34 (2016) 223–229, https://doi.org/10.3857/roj.2016.01816.
[59] P. Gao, N. Li, K. Ji, Y. Wang, C. Xu, Y. Liu, Q. Wang, J. Wang, N. He, Z. Sun, L. Du, Q. Liu, Resveratrol targets TyrRS acetylation to protect against radiation-induced damage, FASEB J. 33 (2019) 8083–8093, https://doi.org/10.1096/fj.201802474RR.
[60] P.G.S. Prasanna, H.B. Stone, R.S. Wong, J. Capala, E.J. Bernhard, B. Vikram, C. N. Coleman, Normal tissue protection for improving radiotherapy: where are the gaps? Transl. Cancer Res 1 (2012) 35–48.
[61] E. Khodamoradi, M. Hoseini-Ghahfarokhi, P. Amini, E. Motevaseli, D. Shabeeb, A. E. Musa, M. Najafi, B. Farhood, Targets for protection and mitigation of radiation injury, Cell Mol. Life Sci. 77 (2020) 3129–3159, https://doi.org/10.1007/s00018-020-03479-x.
[62] E. Obrador, R. Salvador-Palmer, J.I. Villaescusa, E. Gallego, B. Pellicer, J. M. Estrela, A. Montoro, Nuclear and radiological emergencies: biological effects, countermeasures and biodosimetry, Antioxidants 11 (2022) 1098, https://doi.org/10.3390/antiox11061098.
[63] E. Obrador, R. Salvador, J.I. Villaescusa, J.M. Soriano, J.M. Estrela, A. Montoro, Radioprotection and radiomitigation: from the bench to clinical practice, Biomedicines 8 (2020) 461, https://doi.org/10.3390/biomedicines8110461.
[64] J.S. Thompson, Y. Chu, J. Glass, A.A. Tapp, S.A. Brown, The manganese superoxide dismutase mimetic, M40403, protects adult mice from lethal total body irradiation, Free Radic. Res 44 (2010) 529–540, https://doi.org/10.3109/10715761003649578.
[65] G.P. Holmes-Hampton, V.P. Kumar, K. Valenzia, S.P. Ghosh, FSL-1: A synthetic peptide increases survival in a murine model of hematopoietic acute radiation syndrome, Radiat. Res 201 (2024) 449–459, https://doi.org/10.1667/RADE-23-00142.1.
[66] J. Yoshino, J.A. Baur, S. Imai, NAD+ intermediates: The biology and therapeutic potential of NMN and NR, Cell Metab. 27 (2018) 513–528, https://doi.org/10.1016/j.cmet.2017.11.002.
[67] N. Braidy, Y. Liu, NAD+ therapy in age-related degenerative disorders: a benefit/risk analysis, Exp. Gerontol. 132 (2020) 110831, https://doi.org/10.1016/j.exger.2020.110831.
[68] F. Marte, P. Sankar, P. Patel, M. Cassagnol, Captopril, in: StatPearls, StatPearls Publishing, Treasure Island (FL), 2025. ⟨http://www.ncbi.nlm.nih.gov/books/NBK535386/⟩ (accessed July 11, 2025).
[69] E.C. Cheung, K.H. Vousden, The role of ROS in tumour development and progression, Nat. Rev. Cancer 22 (2022) 280–297, https://doi.org/10.1038/s41568-021-00435-0.
[70] Z. Mei, X. Zhang, J. Yi, J. Huang, J. He, Y. Tao, Sirtuins in metabolism, DNA repair and cancer, J. Exp. Clin. Cancer Res 35 (2016) 182, https://doi.org/10.1186/s13046-016-0461-5.
[71] A.R. Michmerhuizen, A.M. Pesch, L. Moubadder, B.C. Chandler, K. Wilder-Romans, M. Cameron, E. Olsen, D.G. Thomas, A. Zhang, N. Hirsh, C.L. Ritter, M. Liu, S. Nyati, L.J. Pierce, R. Jagsi, C. Speers, PARP1 Inhibition radiosensitizes models of inflammatory breast cancer to ionizing radiation, Mol. Cancer Ther. 18 (2019) 2063–2073, https://doi.org/10.1158/1535-7163.MCT-19-0520.
[72] Y. Matsuno, Y. Atsumi, M. Alauddin, M.M. Rana, H. Fujimori, M. Hyodo, A. Shimizu, T. Ikuta, H. Tani, H. Torigoe, Y. Nakatsu, T. Tsuzuki, M. Komai, H. Shirakawa, K. Yoshioka, Resveratrol and its related polyphenols contribute to the maintenance of genome stability, Sci. Rep. 10 (2020) 5388, https://doi.org/10.1038/s41598-020-62292-5.
[73] S. Wu, J. Ren, W. Qian, M. Gong, J. Li, T. Qin, S. Zhang, W. Zhang, H. Sun, Z. Wu, Z. Wang, Q. Ma, W. Duan, Synergistic effects of resveratrol with gemcitabine in pancreatic cancer chemotherapy by inhibiting the c-Met/PARP1 axis, J. Pancreatol. 7 (2024) 267, https://doi.org/10.1097/JP9.0000000000000160.
[74] C.A. Clara, S.K.N. Marie, J.R.W. de Almeida, A. Wakamatsu, S.M. Oba-Shinjo, M. Uno, M. Neville, S. Rosemberg, Angiogenesis and expression of PDGF-C, VEGF, CD105 and HIF-1α in human glioblastoma, Neuropathology 34 (2014) 343–352, https://doi.org/10.1111/neup.12111.
[75] J. Dewangan, S. Srivastava, S. Mishra, A. Divakar, S. Kumar, S.K. Rath, Salinomycin inhibits breast cancer progression via targeting HIF-1α/VEGF mediated tumor angiogenesis in vitro and in vivo, Biochem Pharm. 164 (2019) 326–335, https://doi.org/10.1016/j.bcp.2019.04.026.
[76] X. Jin, Y. Kuang, L. Li, H. Li, T. Zhao, Y. He, C. Di, J. Kang, L. Yuan, B. Yu, Q. Li, A positive feedback circuit comprising p21 and HIF-1α aggravates hypoxia-induced radioresistance of glioblastoma by promoting Glut1/LDHA-mediated glycolysis, FASEB J. 36 (2022) e22229, https://doi.org/10.1096/fj.202101736R.
[77] F. Marampon, G.L. Gravina, B.M. Zani, V.M. Popov, A. Fratticci, M. Cerasani, D. Di Genova, M. Mancini, C. Ciccarelli, C. Ficorella, E. Di Cesare, C. Festuccia, Hypoxia sustains glioblastoma radioresistance through ERKs/DNA-PKcs/HIF-1α functional

interplay, Int J. Oncol. 44 (2014) 2121–2131, https://doi.org/10.3892/ijo.2014.2358.
[78] H. Shen, E. Hau, S. Joshi, P.J. Dilda, K.L. McDonald, Sensitization of glioblastoma cells to irradiation by modulating the glucose metabolism, Mol. Cancer Ther. 14 (2015) 1794–1804, https://doi.org/10.1158/1535-7163.MCT-15-0247.
[79] W. Zhao, H. Hu, Q. Mo, Y. Guan, Y. Li, Y. Du, L. Li, Function and mechanism of combined PARP-1 and BRCA genes in regulating the radiosensitivity of breast cancer cells, Int J. Clin. Exp. Pathol. 12 (2019) 3915–3920.